MAGNETOMOTIVE OPTICAL COHERENCE ELASTOGRAPHY FOR BIOMEDICAL APPLICATIONS

BY

VASILICA CRECEA

DISSERTATION

Submitted in partial fulfillment of the requirements
for the degree of Doctor of Philosophy in Physics
in the Graduate College of the
University of Illinois at Urbana-Champaign, 2015

Urbana, Illinois

Doctoral Committee:

Professor John D. Stack, Chair
Professor Stephen A. Boppart, Director of Research
Associate Professor Karin A. Dahmen
Associate Professor Gabriel Popescu

ABSTRACT

This thesis presents a new non-invasive optical method for assessing biomechanical properties of tissues and cells in real time and with micron scale resolution, magnetomotive optical coherence elastography (MM-OCE). Biomechanical properties are important because they relate to the tissues' state of health and they can be utilized for monitoring changes due to pathological processes or therapeutic treatments. In optical coherence tomography (OCT), the imaging technique that MM-OCE is based on, near infrared light penetrates a few millimeters into highly scattering biological tissues and the backscattered light is detected in real time with interferometry. Post-processing of the optical signal renders structural images and displacement maps of dynamic processes within the specimens, which contain information about the mechanical signature of the tissues or cells. MM-OCE utilizes magnetic nanoparticles or microspheres that are embedded in the samples of interest, and which induce motion in the samples in the presence of an external magnetic field produced by a custom built solenoid coil. Three studies are presented: the first one introduces the MM-OCE technology and demonstrates its feasibility and versatility on a set of tissue-mimicking silicone phantoms, the second one applies MM-OCE to excised rabbit tissues and reveals their intricate biomechanical behavior, and the third one explores the possibility of extending the technique to the study of cells. Finally, I discuss aspects of this work that can be further advanced by future modeling of the biomechanical properties of different types of soft tissue.

ACKNOWLEDGMENTS

The work presented here would not have been possible without the invaluable contribution of many individuals to whom I am forever indebted.

First and foremost, I have a great amount of gratitude for my advisor, Prof. Stephen A. Boppart, for sharing his broad expertise, guiding me, being a brilliant writer, and being patient and understanding throughout the entire course of my graduate studies in the Biophotonics Imaging Laboratory at the Beckman Institute for Advanced Science and Technology. Being a part of his group has been a great privilege. Thank you for this opportunity.

I would like to thank Prof. John Stack for his support and guidance throughout the past few years – they really made an important difference for me. Prof. Karin Dahmen and Prof. Gabriel Popescu, thank you for taking the time to serve in my committee and for supporting me throughout my graduate school years.

Many thanks for all the members of the group, past and present, who created an engaging and nourishing atmosphere at work and elsewhere. Those with whom I have worked closely on research projects deserve a special mention – thank you, Ben, Adeel, Amy, Tyler, Leon (in no particular order). You all contributed a great deal to my learning and I have thoroughly enjoyed our collaborations. I also had very useful and interesting exchanges of ideas with Steven, Jong, Nathan, Yue (from Prof. Insana's group), Guillermo, Joanne, Cac, Freddy, Dan, Yuan, Fred, Youbo, and Simon. The more I think about it, the more I realize every single group member I ever had a chance to talk to (yes, that's pretty much everyone) left me with a new valuable experience, be it about science, the nitty-gritty of hard/soft-ware, a new exotic dish from a land far, far away, or simply human nature. And through it all, Eric, Marina, and Darold have been the glue that kept us all going – their contributions could not be understated. Thank you, guys! Keep up the good work!

To my friends who have supported me no matter what, you guys are priceless. Chino, no matter wherever and whenever you'll be, I'll know I can count on you. Adeel, you make the cut for this category too. Themis and Meng, you girls rock (not just at Physics!). Without you, graduate school would not have been such a good life school too. Similar credits go out to Joe, Abhi, the Kevinator, Dan V., Soheil, Wladi, Emilie, Akbar, Nasrin, Janice, Debbie, Knut Sr., my sensei, Ana M., Ana R., Jo:rg, Norbi, Roxy, Pato, Maro, Andrei, Jess, Elena, Tanveer, Anupama, Florin, Pylot, and Charles. You've made my life so much better.

Vikram, thanks for your poetry. In you I found a rare literary mirror. You should keep writing. Thanks for sharing your mind with me.

Mom and dad, thanks for your support and care. I wouldn't be here without them. Getu, thanks for keeping an eye on me and giving me strength. I'm so happy that because of you I'm four-fold an aunt. My life is so much better for being part of the same family as Ştefan, Tudor, Vlad, and Matei.

Not at last, many thanks for the family of Linda Su-Nan Chang Sah for their generous support in providing the funding for the fellowship by the same name that I was fortunate to receive for three years during my graduate studies.

TABLE OF CONTENTS

1 INTRODUCTION....1
1.1 Background and motivation....1
1.2 Elastography methods....3
1.3 Optical elastography....4
1.4 Optical coherence tomography....5
1.5 Magnetomotive optical coherence elastography (MM-OCE)....8
2 MAGNETOMOTIVE OPTICAL COHERENCE ELASTOGRAPHY OF SILICONE SAMPLES....13
2.1 Introduction....13
2.2 Methods and results....14
2.3 Discussion....21
3 MAGNETOMOTIVE OPTICAL COHERENCE ELASTOGRAPHY FOR MICRORHEOLOGY OF BIOLOGICAL TISSUES....26
3.1 Introduction....26
3.2 Methods....27
3.2.1 Tissue specimen preparation....27
3.2.2 Imaging system....27
3.2.3 Data acquisition....28
3.2.4 Data analysis....28
3.3 Results and discussion....30
4 MAGNETOMOTIVE OPTICAL COHERENCE MICROSCOPY FOR CELLULAR BIOMECHANICS....37
4.1 Introduction....37
4.2 Methods....40
4.2.1 Cell sample preparation....40
4.2.2 Imaging system....41
4.3 Results of magnetic microspheres study....46
4.4 Cellular biomechanics utilizing magnetic nanoparticles....51
4.5 Discussion....55
5 CONCLUSIONS AND OUTLOOK....60
6 REFERENCES....66

1 INTRODUCTION

In this thesis magnetomotive optical coherence elastography (MM-OCE) is introduced, a functional imaging technique where magnetic nanoparticles are embedded in the specimens to be imaged and, upon excitation with an external magnetic field, trigger motion in the surrounding specimen, and the resulting nanoscale displacements are measured with phase-resolved spectral domain optical coherence tomography. Biomechanical parameters of specimens of interest are directly measured this way.

1.1 Background and motivation

There has been a great deal of interest in imaging structure and function of specimens in biology and medicine, as well as in other science fields such as materials science, physics, geology, chemistry, etc. Non-destructive, minimally invasive visualization in real time and with high resolution has been a main goal in engineering new tools that would allow unprecedented observations that would offer insight into the inner workings of nature's processes.

Optical coherence tomography (OCT) is an established biomedical imaging modality in the near-infrared range that uses low-coherence interferometry for non-invasive high-resolution measurements of morphological and functional features of biological samples in real time, both *in vitro* and *in vivo* [1]. Existing OCT methods rely on retrieval of object structure and dynamical information from the amplitude or the phase of the backscattered light. OCT benefits from a variety of contrast agents that enhance

imaging contrast in the samples under study by local differentiation via different mechanisms, such as external mechanical modulation or change in optical properties (either scattering or absorption) [1, 2].

In this study the focus is on a class of magnetic contrast agents whose magnetic susceptibility is a few orders of magnitude higher than that of biological tissues, and thus yields high contrast in OCT images. The magnetic agents are controlled in a way that is not harmful to the specimen, by applying an external magnetic field gradient. The goal is to improve the imaging performance and sensitivity of detection in biological samples probed with these contrast agents, in a spectral-domain OCT system and using phase measurements. The results detailed in the following chapters of the thesis show the versatility of this technique for studies of micromechanical properties of tissue samples and cells, rendering information that could potentially be utilized to diagnose the health of these specimens.

The biomechanical properties of tissues and cells are known to contain information about the state of health of the organs or organism where they reside. A well-known example is the physical palpation of the skin surface and underlying tissue structures to determine their gross biomechanical properties in relation to adjacent regions of tissue. A small local hardening in the breast is often found in a number of pathologies, from benign sebaceous cysts to malignant breast cancer. Thus, there is a great deal of interest in having access to versatile diagnostic tools that could differentiate pathological tissue from normal tissue in unique ways.

1.2 Elastography methods

Elastography is a functional extension of medical imaging where the elastic/mechanical properties of a sample are imaged [3]. The mechanical properties of biological specimens are widely known to be correlated with the progression of disease [4]. Biological tissues are known to have a viscoelastic behavior. Viscoelastic materials, as their name suggests, have both elastic and viscous properties. Namely, they store a portion of the energy they receive from external sources as potential energy, while the other portion is damped [5-9]. Their mechanical properties are of crucial importance for their function and reliability.

Current methods for the measurement of mechanical properties of viscoelastic materials include ultrasound elastography [8, 10-12], magnetic resonance elastography (MRE) [13-16], vibro-acoustography [17, 18], atomic force microscopy (AFM) [19], and optical coherence elastography [20-26]. These methods are either static or dynamic, and aim to detect displacements in samples when an external or internal stress is applied. Computational cross-correlation algorithms are often employed for tracking image features or pixels, and used for mapping their displacement [14, 20]. Unfortunately, these algorithms are prone to error in accurately measuring displacements and tracking of scatterers [14]. The inability to obtain quantitative measurements and the need for reference samples that yield relative measurements are some of the more common disadvantages of some of these techniques.

Elastography imaging systems typically require high cost and long data acquisition and processing times [10-19]. A more traditional technique for measuring mechanical properties of samples is indentation, wherein controlled mechanical pressure is applied to samples with well-defined geometries and the strain-stress curves are used for inferring the bulk elastic moduli of the probed samples [4]. Elastography and rheology, both well-established fields, have been greatly advanced by new technologies for characterizing material properties, and in particular, viscoelastic parameters. These advances have been limited, however, by challenges such as resolution or the need to isolate the samples for measurements. The need for an inexpensive, real-time, non-contact, non-destructive, and quantitative method for the assessment of highly localized micromechanical properties with few constraints on the geometry or dimensions of the samples is apparent.

1.3 Optical elastography

A number of methods have been reported to assess the biomechanical properties of tissues using optical methods. The high spatial resolution possible with optical methods offers the ability to provide greater displacement sensitivity compared to other elastography techniques based on ultrasound and MRE [22]. Optical coherence elastography (OCE) has been recognized as a versatile approach for measuring and mapping biomechanical properties of biological tissues on the micron scale [3, 27-33]. OCE measurements have been used to assess the biomechanical properties of a wide variety of tissues of interest, such as measuring the stiffness of arteries [34], different skin layers [35], tissue engineering constructs [36] and the cornea [37, 38]. OCE requires the

application of a mechanical load (stress) on the sample, and by measuring the resulting displacements, the viscoelastic properties of the sample can be extracted. Mechanical stresses are induced in the samples of interest through either dynamic or static methods. In dynamic methods, the excitation source could be external, such as mechanical compression using piezoelectric (PZT) actuators [39-41], or it could be an internal excitation, such as by using acoustic radiation force to displace the internal tissue structures [42, 43]. Various methods could be used to quantify the displacement of the tissues. Earlier methods for elastography using OCT relied on speckle-tracking algorithms to estimate tissue displacement, however, speckle de-correlation and spatial sampling limit the range of displacements that can be reliably measured [44]. Phase-resolved measurements, where the axial displacements are tracked based on the phase difference between adjacent A-scans, have been more widely employed to estimate small scale displacements [33]. The lower and upper limit on the displacement range using phase-resolved methods depends on the phase noise and phase wrapping, respectively. Some research groups have also used shear wave propagation [43] or surface acoustic waves [45] in tissue samples to measure the stiffness of the tissue.

1.4 Optical coherence tomography

Optical coherence tomography (OCT) forms depth-resolved images by interferometrically detecting the backscattered light from a sample [1, 46]. In principle OCT is very similar to ultrasound but instead of sound waves low coherence light is utilized. The light from a source is split into two arms, reference arm and sample arm, by a fiber optic coupler. The light in the sample arm is focused into the sample by a focusing

lens and is backscattered from different structures within the sample. This backscattered light combines with the light from the reference arm and forms an interference pattern. This interference pattern is detected by a spectrometer and further processed to generate a single axial-scan (a column in an OCT image). The beam is then scanned over the sample to generate two or three dimensional OCT images. The laser light used in OCT is in the near infrared regime in the so-called biological window (~700 nm – 1300 nm) where the light-tissue interaction is dominated by scattering rather than absorption. The penetration depth in OCT is limited by multiple scattering and, in highly scattering biological tissue, is around 1-2 mm. The axial and transverse resolutions in OCT are independent of each other. The axial resolution in OCT depends on the bandwidth of the laser source while the transverse resolution is dependent on the numerical aperture of the focusing lens in the sample arm.

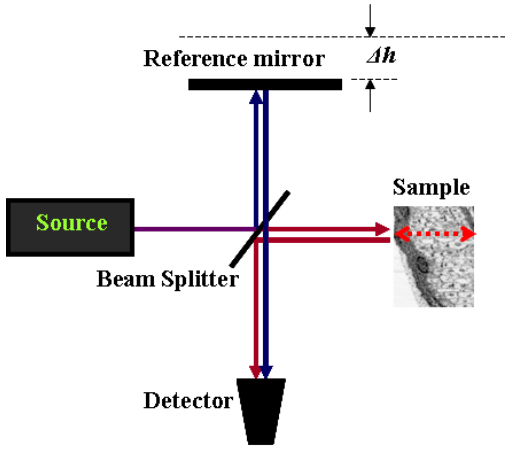

Figure 1.1 Representative experimental set-up for a time-domain OCT system. Δh represents the distance the reference mirror is moved in order to image an equal depth in the sample.

Image reconstruction is based on the theory of inverse scattering; by inverse Fourier-transforming the autocorrelation signal from the demodulated detected intensity

at different times (time-domain OCT, Fig. 1.1) or wavelengths (spectral-domain OCT), one can retrieve the complex analytic signal that contains amplitude and phase information about the object. For interference to occur in time-domain OCT, the optical paths of the reference and the sample arms need to differ by no more than the coherence length l_c of the source. This also sets the limit on the axial resolution of the system, which is equal to l_c. For a Gaussian probing spectrum, l_c is inversely proportional to the bandwidth $\Delta\lambda$ of the source, as shown in equation (1.1). Therefore, the use of a very broad bandwidth source for high axial resolution imaging is desired. The transverse resolution R_T is given by the diameter of the probing beam $2w_0$ and can be expressed in terms of the focal length f of the focusing lens, the center wavelength of the source λ_0, and the diameter of the focused beam D, incident on the lens (assuming a Gaussian probing beam), as shown in equation (1.2).

$$l_c = 0.44\frac{\lambda_0^{\,2}}{\Delta\lambda} \tag{1.1}$$

$$R_T = 2\omega_0 = 2.44\frac{f\lambda_0}{D} \tag{1.2}$$

OCT, when compared to other established medical imaging modalities such as ultrasound and MRI, offers a much higher resolution. However, the tradeoff is much smaller penetration depth and field of view. The real-time, high resolution, and depth resolved imaging capabilities of OCT have found wide spread applications in numerous areas of biology and medicine such as in ophthalmology, cardiology, and dermatology, among many others [1].

1.5 Magnetomotive optical coherence elastography (MM-OCE)

Several classes of contrast agents have been shown to benefit OCT. Magnetic nanoparticles (MNPs) are promising candidates for contrast agents in biomedical imaging [2, 47-49], and in particular for OCT [2, 47, 49], due to their versatility and compliance with biosafety requirements. Superparamagnetic iron oxide (SPIO) nanoparticles have already been used extensively as contrast agents for MRI [50]. Nanoparticles with small core sizes (less than 20 nm) are easily transported through the circulatory system and are able to extravasate, and are thus suitable for both *in vivo* and *in vitro* studies [2, 50]. Depending on their composition and size, nanoparticles can be very responsive to external, non-invasive manipulation or detection due to their strong magnetic susceptibility, which is five orders of magnitude higher than that of biological tissues. Moreover, they can be functionalized to target antigens and thus enhance contrast at the molecular and cellular level, aiding in pathology localization and early diagnosis of disease. Reliable and sensitive methods for characterizing the response of the magnetic nanoparticles to magnetic fields and that of the surrounding biological medium are presently needed.

In elastography, externally-applied mechanical stresses using a load cell or piezoelectric actuators tend to be large in scale and coverage, which may limit the high-resolution mapping of the mechanical properties. MNPs were employed in this study for dynamic mechanical actuation as these could provide localized mechanical perturbations enabling the high-resolution probing of the tissue viscoelastic properties. Their small size allows them to diffuse through the tissues of interest, thereby allowing these to be used as local

probes to assess the local mechanical environment of the tissues. It has been previously shown that they can enhance the contrast in OCT images [51] and can be effective transducers for sensitive MM-OCE measurements [52]. By measuring the response of the tissue to a step excitation at high spatial and temporal resolution, a new way of simultaneously measuring several biomechanical parameters of interest, such as the elastic modulus, tissue displacement rise time, creep factor, and the natural frequency of biological tissues, is proposed.

When embedded in tissue that is subsequently probed with an external magnetic field, magnetic nanoparticles that are far from saturation move along the axis on which the field $\boldsymbol{B}$ has a dominant gradient, as it follows from the force equation:

$$F_p = \frac{V_p\left(\chi_p - \chi_{bg}\right)\nabla B^2}{2\mu_0}, \tag{1.3}$$

where F_p is the magnetic force acting on a magnetic nanoparticle with volume V_p and magnetic susceptibility χ_p, χ_{bg} is the magnetic susceptibility of the background sample, and μ_0 is the space permeability [47]. The sample arm and the electromagnet coil/solenoid are positioned such that the magnetic field at the site being probed/imaged has a dominant vertical component (that is also parallel to the probing beam) along which it varies, engaging the magnetic nanoparticles in motion on this direction and creating magnetomotive contrast, as shown in Fig. 1.2. Magnetomotive optical coherence tomography (MM-OCT) in a time-domain OCT (TD-MMOCT) system has been used for detecting the displacements in different samples caused by the modulation of the magnetic field and it has been subsequently shown that the magnetomotive response in the system is predictable [2]. In this scheme, axial scans in

a two-dimensional transversal sample plane were acquired with the magnetic field off and on, while allowing the particles and the sample sufficient time to complete motion and reach equilibrium between axial scans. Thus, the images taken with the time-domain MM-OCT system represent a static description of the sample in the absence and in the presence of the magnetic field. Experimental verification relied on analysis of amplitude changes that revealed magnetic field-induced motion in the samples of interest. This MM-OCE study explores phase detection as an alternative, more sensitive method of detection of magnetomotive displacements.

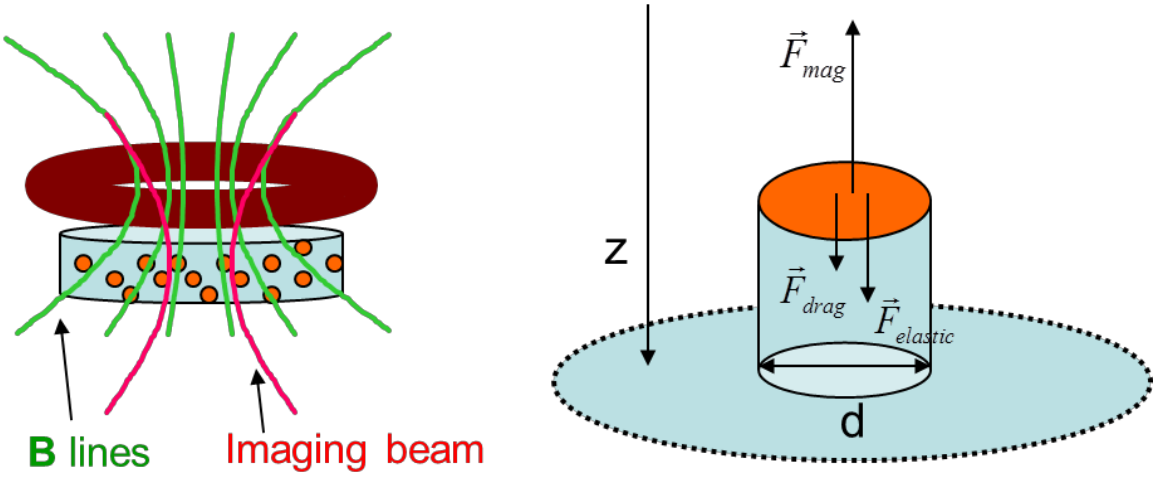

Figure 1.2 Schematic of: (Left) sample with electromagnet coil and (Right) single MNP and forces acting on it. **z** is the imaging axis and d is the diameter of an MNP; the elastic, drag, and magnetic forces acting on the MNP are indicated by the respective vectors.

Phase measurements in common-path low-coherence light interferometry have been shown to render high sensitivity to sub-wavelength displacements or obstacles in the path of light [53, 54]. Path length sensitivities as low as 25 pm for spectral-domain optical coherence phase microscopy (SD-OCPM) [55] and 18 pm (equivalent phase stability = 0.4 mrad) for spectral-domain phase microscopy (SDPM) [53] have been

reported. Phase-resolved methods [56-58] are often used in a dynamic regime, such as in measuring intralipid [59-61] or blood flow [62-66] velocities, nerve displacements [67], or monitoring cell activity [55]. These remarkable results suggest that phase measurements in a spectral-domain OCT system are an appropriate approach for studying the magnetomotion in MMOCT.

Studying the dynamics of the magnetic nanoparticles could shed light onto the micromechanical properties of the tissue that hosts them and thus extend the capabilities of OCT to elastography. The tissue exerts a restoring elastic force and a viscous drag force that oppose the magnetic force on the nanoparticles of mass *m*,

$$|\vec{F}_{elastic}| = E(\Delta z / z_0)(\pi d^2 / 4) \tag{1.4}$$

$$|\vec{F}_{drag}| = 3\pi d\eta(\partial z / \partial t), \tag{1.5}$$

where d is the diameter of the nanoparticle and E and η are the elastic modulus and the viscosity, respectively, of the sample medium at the location of the nanoparticle. From Newton's second law and the force expressions above, the equation of motion of the MNP is obtained, which turns out be the equation of a damped oscillator:

$$z'' + \beta z' + \omega_0^2 z = 0. \tag{1.6}$$

z is the vertical axis, and also the direction of motion of the MNP. When

$$\beta^2 - 4\omega_0^2 < 0 \tag{1.7}$$

the oscillation is underdamped (for critical damping the expressions evaluates to 0, and for overdamping it is positive). With MM-OCE, it is possible to measure the damping factor β and the resonant frequency ω_0. Thus, the regional elastic properties of the

sample on the micron scale, and throughout its volume, can be inferred [2].

When the nanoparticles displace in response to the magnetic field activity, they also engage the surrounding tissue in movement. The phase changes $\Delta\varphi$ in the complex analytic signal are related to the displacements Δz in the sample by the equation:

$$\Delta\varphi = \frac{4\pi}{\lambda_0}\Delta z. \tag{1.8}$$

Thus one can easily calculate the displacement from the measured phase differences can be easily calculated.

In order to study the dynamics of the magnetomotion one needs to take advantage of the capabilities of a spectral-domain OCT system: fast acquisition rates, good phase stability for increased sensitivity of detection (the reference-arm mirror is fixed, unlike in TD-OCT systems), and, not least, better signal to noise ratios [68-71].

The rest of the dissertation is organized as follows. In Chapter 2 I demonstrate the proof of principle of MM-OCE using tissue-mimicking phantoms while in Chapter 3 I extend this method to biological specimens. In chapter 4 I explain the adaptation of MM-OCE to study cellular biomechanics. Finally, I summarize this work and outline some future directions in chapter 5.

2 MAGNETOMOTIVE OPTICAL COHERENCE ELASTOGRAPHY OF SILICONE SAMPLES[1]

2.1 Introduction

The availability of a real-time non-destructive modality to interrogate the mechanical properties of viscoelastic materials would facilitate many new investigations. In this chapter, I introduce a new optical method for measuring elastic properties of samples which employs magnetite nanoparticles as perturbative agents. Magnetic nanoparticles distributed in silicone-based samples are displaced upon probing with a small external magnetic field gradient and depth-resolved optical coherence phase shifts allow for the tracking of scatterers in the sample with nanometer-scale sensitivity. The scatterers undergo underdamped oscillations when the magnetic field is applied step-wise, allowing for the measurement of the natural frequencies of oscillation of the samples. Validation of the measurements is accomplished using a commercial indentation apparatus to determine the elastic moduli of the samples. This real-time non-destructive technique constitutes a novel way of probing the natural frequencies of viscoelastic materials in which magnetic nanoparticles can be introduced.

In this study I introduce a novel optical elastography technique, MM-OCE, based on phase-resolved spectral-domain OCT [69], which affords the capability of imaging non-invasively, non-destructively, and in real time. By introducing MNPs in the medium to

[1] Crecea V, Oldenburg AL, Liang X, Ralston TS, Boppart SA. Magnetomotive nanoparticle transducers for optical rheology of viscoelastic materials. Optics Express, 17:23114-23122, 2009.

be probed, and by applying a small, controlled, external magnetic field, one gains access to the nano- to micro-level interactions between the MNPs and the surrounding microenvironmental matrix [47, 72].

Micromechanical properties of samples can be determined from dynamic measurements when a controlled modulated mechanical response is triggered in the sample [2, 30, 47, 73]. Magnetomotion is induced in silicone-based samples via the interaction of a small localized external magnetic field with MNPs distributed in the samples. This novel technique combines the advantages of localized magnetomotive contrast on the micron scale with fast real-time depth-resolved optical imaging to quantify the dynamic micromechanical properties of viscoelastic materials. Magnetomotive optical coherence elastography is conceptually different from magnetomotive OCT (MM-OCT) [2, 30, 47] because it quantitatively measures the time-dependent oscillations of MNPs and their surrounding microenvironment, and uses this information to determine the viscoelastic properties of the medium. In contrast, MM-OCT only uses the MNP modulation as a means for contrast enhancement in OCT.

2.2 Methods and results

In order to assess the validity of MM-OCE for measuring dynamic elastic properties of materials with different stiffness, I examined a set of polymer-based samples with elastic mechanical properties that spanned a wide range. Polydimethylsiloxane (PDMS)-based samples with optical and mechanical properties representative of soft polymers, composites, and biological tissues were prepared [74]. To vary the elasticity of the samples, the ratio (PDMS):(curing agent RTV 615 A) was varied in the range 25:1-10:1,

while the relative ratio of the curing agent and the crosslinker, RTV 615 A:RTV 615 B, was maintained at 10:1 for all samples. Titanium dioxide (TiO_2) microparticles (Sigma-Aldrich, #224227, average diameter 1 μm, < 5 μm) with a concentration of 4 mg/g served as optical scatterers and magnetite MNPs (average diameter 25 nm, Sigma-Aldrich, #637106) with a concentration of 2 mg/g served as magnetomotive perturbative agents. The average distance between the TiO_2 particles was 10 μm and 200 nm between MNPs. The polymers and the TiO_2 particles were thoroughly mixed with the aid of a magnetic stir plate. Subsequently, the MNPs were added and the sample solution was homogenized in an ultrasonic sonicator for five hours. They were then poured into Petri dishes with a diameter of 38 mm and a height of 5 mm, curing 12 hrs at 80°C, and subsequently 24 hr at room temperature (22 °C). An indentation instrument (model TA.XT Plus Texture Analyzer, Texture Technologies Corp., Algonquin, IL) was used for independent validation measurements of the elastic moduli of the samples.

The composition of these samples was varied, resulting in noticeable (by palpation) differences in their elasticity. As confirmed by indentation measurements using a commercial indentation instrument, the static elastic moduli of these samples ranged from 0.4-140 kPa. The concentration of optical scatterers and MNPs as well as the geometry and dimensions of all samples were kept constant. In this study, the MNPs are believed to be mechanically bound directly to the solid polymer matrix of the silicone medium. The consistency and repeatability of the MM-OCE measurements support this hypothesis.

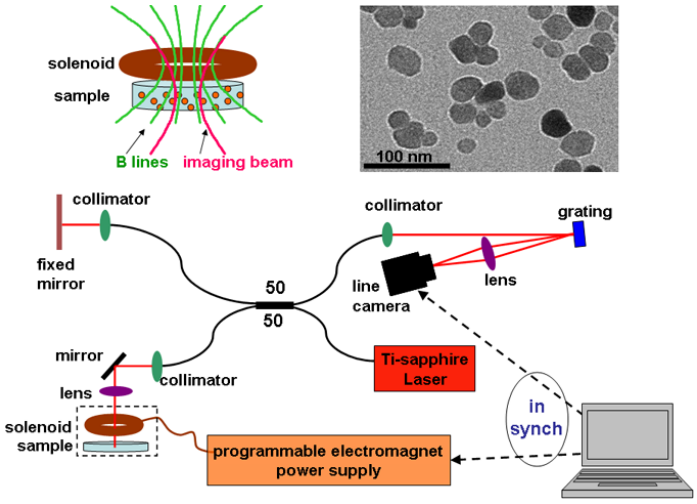

Figure 2.1 Schematic diagram of the MM-OCE set up with MNPs. (top left) The magnetic coil provides a magnetic field that is aligned axially with the imaging beam. The field gradient engages the motion of MNPs in the sample. (top right) Transmission electron micrograph of the magnetite MNPs. (bottom) The near-infrared light provided by the titanium:sapphire laser is divided by the 50:50 fiber-optic beamsplitter between the reference and the sample arms of the interferometer. The interference signal is wavelength-dispersed by a diffraction grating and recorded by a charged coupled device (CCD) line array. The magnetic field activity is synchronized with the OCT data acquisition, and the resulting optical back-scattering data is acquired, processed, and displayed on a personal computer.

A spectral-domain OCT system [30] was used to perform real-time interferometric imaging of the samples. The sample arm was modified to accommodate a small electromagnetic coil custom-designed to optimize the magnetic field gradient within the focal region of the optical imaging system, as illustrated in Fig. 2.1. The probing light was provided by a Nd:YVO_4-pumped titanium:sapphire laser (KMLabs, Boulder, CO) with a center wavelength of 800 nm and a bandwidth of 120 nm, providing an axial resolution of 3 μm in the samples. The average power incident on the samples was 10 mW. A 40 mm focal length lens was used to focus the light in the sample arm to a 16 μm spot (transverse resolution). Magnetic field modulation was synchronized with

optical data acquisition. M-mode imaging data was acquired at a camera line rate of 29 kHz (34 µs per axial depth scan) for a total acquisition time of 280 ms per M-mode image. During the acquisition of each image the magnetic field was turned on shortly after the start of the acquisition and kept constant for 100 ms, and then switched off in a square-wave pattern, releasing the MNPs and resulting in the relaxation of the sample, as illustrated in Fig. 2.2.

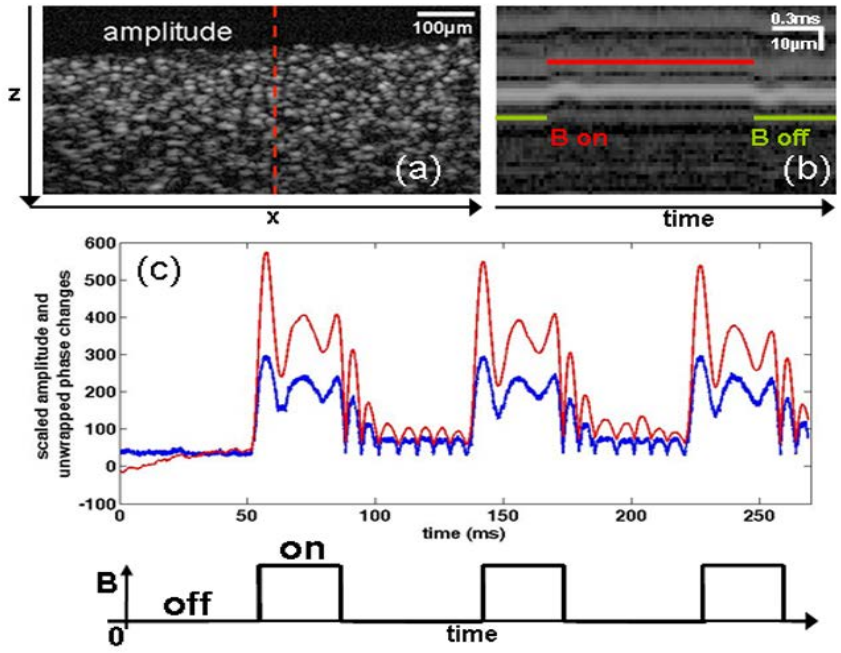

Figure 2.2 Scatterer response upon step-wise modulation of a magnetic field. (a) Two-dimensional (x-z) cross-sectional (B-mode) amplitude OCT image of a silicone sample containing MNPs and TiO_2 optical scatterers. The dashed line indicates the location in the sample where M-mode imaging was performed with MM-OCE. (b) M-mode amplitude OCT image of a region of scatterers acquired while the magnetic field was applied step-wise. (c) Average time-dependent scatterer changes along one axial position, illustrating both the changes in phase (red) and changes in amplitude (blue) as the magnetic field is applied step-wise, relative to an idle state with zero magnetic field.

The complex analytic signal obtained from the raw optical data acquired in M-mode was used to extract the phase associated with individual scatterers in the samples (at fixed positions in depth) as a function of time. The phase variation was recorded as the magnetic field was applied step-wise to the sample, and the absolute displacement of the scatterers was deduced from Eq. (1.7) [75]. Based on the parameters of our system and of our samples, the displacement can be calculated directly from this equation. The displacement sensitivity of the system, defined as the standard deviation of the measured position of a stationary mirror in the sample arm, was 11 nm. Typical maximum displacements measured in the samples were in the order of a few hundred nanometers.

Within 2-20 ms after the onset of the magnetic field, the scatterers were observed to reach a maximum displacement. This was followed by an underdamped oscillation that eventually settled to a new static position as the scatterers reached equilibrium (Fig. 2.2). A similar behavior was observed when the field was removed and the MNPs in the sample were released from the magnetic force and allowed to return to their initial equilibrium position as a result of the binding/restoring force on the MNP from the microenvironment.

The requirement for the linearity of the viscoelastic material behavior is that the displacements induced be at most 0.2% of the length of the sample [76]. In this study, the height of the samples was 5 mm, and therefore displacements of at most 10 μm would ensure a linear response and predict direct proportionality of natural frequencies with the square root of the elastic moduli. Moreover, in order to avoid confounding phase

unwrapping, displacements did not exceed half the axial resolution of the OCT system, namely 1.5 μm. Therefore, the strength of the magnetic field was adjusted in the range of 100-600 Gauss for samples with different elasticities to ensure that this maximum displacement was not exceeded. The graph in Fig. 2.3 shows the variation of the maximum phase change and displacement in a representative sample (with an (RTV A):(RTV B) ratio of 10:1, a concentration of 2.5 mg/g of MNPs, 4 mg/g TiO_2 and with a measured elastic modulus of 3.1 kPa) as the magnetic field strength is increased.

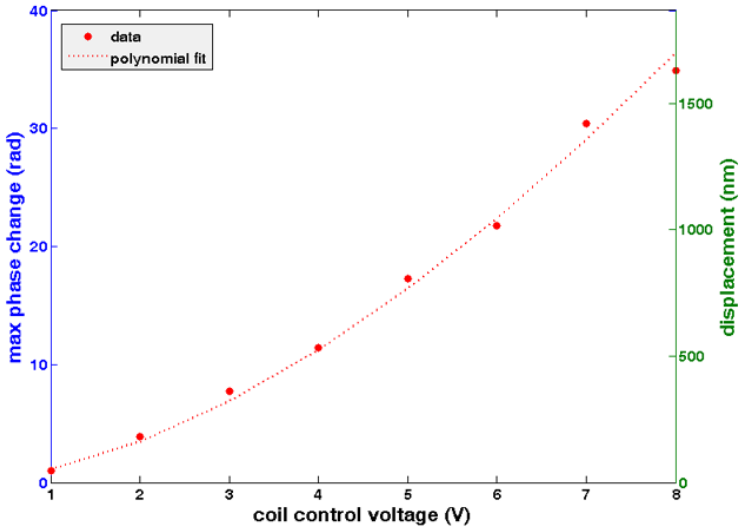

Figure 2.3 Scatterer response to different magnetic field strengths. Direct measurements (points) of maximum change in unwrapped phase from an average scatterer, which are directly proportional to the average maximum displacements of the MNPs, as the electromagnet control voltage is changed. The polynomial fit follows the law $y=Cx^{1.7}$. The applied voltage is directly proportional to the gradient of the square of the magnetic field. MM-OCE data is acquired at displacements not exceeding 1.5 μm in order to avoid excessive phase wrapping of the phase signal.

The natural frequency of oscillation of each sample was obtained from the time-resolved displacement of each scatterer, measured optically with the coherence ranging system.

The displacement curves of the scatterers were fitted to the equation of motion of an underdamped oscillator with two frequency components according to equation (2.1):

$$d(t) = \sum_{i=1}^{2} a_i e^{-\pi\gamma_i t} \cos(2\pi f_i t - \delta_i) + C \tag{2.1}$$

where $d(t)$ is the displacement as a function of time, a_1 and a_2 are the amplitudes of the two frequency components, γ_1 and γ_2 are the corresponding damping coefficients, f_1 and f_2 are the frequencies of oscillation, δ_1 and δ_2 are arbitrary phases, and C is a constant. The R-values of the curve fittings were all above 85%. The dominant natural frequencies of oscillation of the samples were plotted against the square root of the elastic modulus.

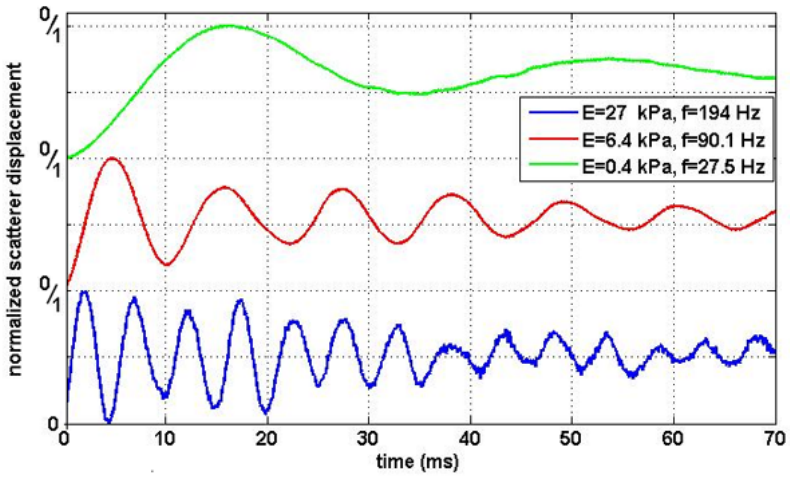

Figure 2.4 Normalized measured displacements from samples of different elastic moduli following a step (off-to-on) transition of the applied magnetic field. Three samples that span a wide range of elastic moduli (measured by indentation: 0.4 kPa [green], 6.4 kPa [red], 27 kPa [blue]) are shown. These sample moduli are characteristic of soft biological tissue, and were chosen to illustrate the natural frequencies of oscillation measured by MM-OCE. The "0/1" labels on the vertical axis are respectively indicating the minimum and maximum of the normalized amplitudes of the displacements traces. As expected, it is observed that as the stiffness of the medium increases, the natural frequency of oscillation of the response increases.

Figure 2.4 illustrates the normalized scatterer traces when the field was applied on three samples with different elastic moduli, as validated by indentation measurements. It is observed that the natural frequency of oscillation varies strongly with the elastic modulus and, as expected, stiffer samples exhibit higher frequencies. Some of the recorded displacement traces have secondary frequency components whose amplitudes are consistently smaller than those of the main frequency components.

2.3 Discussion

Viscoelastic media can often be modeled as a Voigt body [77]. This model predicts a linear relationship between the natural frequency of oscillation of a material and the square root of its elastic modulus. The graph in Fig. 2.5 summarizes the MM-OCE measurements of natural frequencies of oscillation for the range of samples investigated, with elastic moduli varying between 0.4 and 140 kPa, confirming this prediction. The natural frequencies closely follow a linear dependence on the square root of the elastic moduli over this range that spans three orders of magnitude, reinforcing the validity and applicability of MM-OCE for elasticity measurements of various materials.

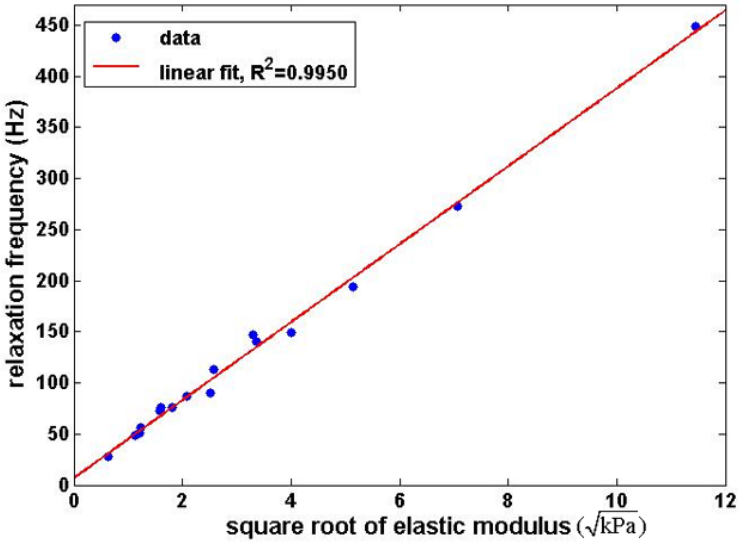

Figure 2.5 MM-OCE-measured natural frequencies of oscillation in samples of varying elastic moduli. The natural frequency of oscillation of the viscoelastic medium depends linearly on the square root of the elastic modulus, as predicted by the Kelvin-Voigt model. The MM-OCE relaxation frequency data (vertical axis) were collected as the samples relaxed following an on-to-off step magnetic field transition. The elastic moduli (horizontal axis) values were measured by indentation.

The range of elastic moduli investigated here was representative of the majority of soft polymer composites and matrices. It should be noted that studies have reported biological tissues also exhibit elastic moduli in a range similar to that investigated in this study, with representative values for adipose tissue (1.9 kPa), breast tumor (12 kPa) [78], and forearm skin (120 kPa) [79]. With the current MM-OCE technology, samples stiffer than 140 kPa exhibited an overdamped response when the magnetic field was applied, and the analysis presented in this study does not apply in such cases. Samples softer than 0.4 kPa are similar to a liquefied gel and their frequencies of oscillation are too low to be measured in real-time with the MM-OCE system. However, the range of elasticities explored herein is representative for many materials of interest, demonstrating that

MM-OCE has the potential for a wide range of investigational and diagnostic studies in materials science, biology, and medicine. MM-OCE requires that the magnetic nanoparticles be present in the samples. The magnetic nanoparticles used in this study, however, had a negligible effect on the bulk elastic modulus of the samples, as demonstrated by measurements with a commercial indentation instrument. Future modeling is needed to more precisely describe the dependence of the natural frequency of oscillation on the elastic modulus while taking into account the interactions between MNPs and their cooperative interactions with the external magnetic field, as well as how the binding of MNPs to the surrounding matrix affects the displacement of scatterers.

MM-OCE benefits from nanometer displacement sensitivity due to phase stability in the optical ranging system and the fact that minute (sub-resolution) displacements of scatterers in the samples result in slight changes in phase. The error in the measurements of the frequencies of oscillation was as small as 0.03% and no larger than 2%. The main noise sources in the MM-OCE system are the small variations of the magnetic field gradient, the scatterer movement in the three-dimensional sample matrix, the optical detection electronics, and the fitting of the displacement traces. Given the high resolution and high sensitivity of the imaging system, MM-OCE can readily measure real-time displacements non-invasively and non-destructively at the micron level, without the requirement of physical contact with the sample. This offers a clear advantage over other mechanical methods that measure stress-strain characteristics and have these limitations.

The minimum concentration of magnetic particles that can be detected with MM-OCT/OCE depends on a number of factors, such as the noise in the OCT system and the magnetic and mechanical properties of the sample and of the MNPs. A previous study using a homogeneous PDMS-based tissue model found that MNP concentrations as low as 27 ug/g can be detected in tissue samples [30]. MM-OCE measurements, however, require the extraction of quantitative parameters form the magnetomotive response; hence, the MM signal levels must be sufficiently higher than the noise floor of the system. This would mean that a higher MNP concentration would be required in MM-OCE compared to MM-OCT, as the MM-OCT measurements merely require the detection of presence (and not necessarily extracting quantitative parameters such as displacement) of MNPs, and can thus tolerate lower SNRs.

Boundary conditions (such as the geometry and the dimensions of a sample) are generally important in assessing the values of elastic moduli. In this study, the boundary conditions were controlled and kept constant for all samples. It has been suggested, however, that dynamic methods for probing mechanical properties have the potential for local characterization regardless of boundary conditions (when the boundaries are relatively far from the point of measurement [10]). Efforts are currently being directed towards the development of analytical models that describe viscoelastic media and the dynamic regime that MM-OCE is probing, as well as towards the investigation of the effect of boundary conditions on the values of the natural frequencies of oscillation.

Phase-resolved methods employed for scatterer tracking in MM-OCE afford real-time nano- to micro-scale measurements, creating the possibility for mapping mechanical properties with high resolution, superior to that of most other rheology technologies. The utilization of MNPs in MM-OCE and their nanometer-scale displacements enables the interrogation of a medium of interest at the nano-level and, given the cooperative action of the MNPs, at the micro-level of the sample. MM-OCE can directly measure natural frequencies of oscillation of various samples. With this versatility, MM-OCE could become a powerful tool with a wide range of applications in materials science.

3 MAGNETOMOTIVE OPTICAL COHERENCE ELASTOGRAPHY FOR MICRORHEOLOGY OF BIOLOGICAL TISSUES[2]

3.1 Introduction

In this chapter, a new development of a spectral domain OCE technique that enables simultaneous measurements of multiple biomechanical parameters of biological tissues is presented. This approach extends the capabilities of MM-OCE, which utilizes iron oxide MNPs distributed and embedded in the specimens as transducers for inducing motion. Step-wise application of an external magnetic field results in displacements in the tissue specimens that are deduced from sensitive phase measurements made with the MM-OCE system. In this study, freshly excised rabbit lung and muscle tissues were analyzed. It is observed that while they present some similarities, rabbit lung and muscle tissue displacements display characteristic differentiating features. Both tissue types undergo a fast initial displacement followed by a rapidly damped oscillation and the onset of creep. However, the damping is faster in muscle compared to lung tissue, while the creep is steeper in muscle. This approach has the potential to become a novel way of performing real time measurements of biomechanical properties of tissues, and to enable the development of new diagnostic and monitoring tools in biology and medicine.

[2] Crecea V, Ahmad A, Boppart SA. Magnetomotive optical coherence elastography for microrheology of biological tissues. J Biomedical Optics, 18:121504, 2013.

3.2 Methods

3.2.1 Tissue specimen preparation

Under a protocol approved by the Institutional Animal Care and Use Committee at the University of Illinois at Urbana-Champaign, tissues were harvested from a New Zealand white rabbit (Covance, Princeton, NJ) and sectioned in cubes with a volume of ~ 3.38 cm^3. The fresh tissues were then completely immersed for 4 hrs in a room temperature saline suspension of MNPs (average diameter 25 nm, Sigma-Aldrich, #637106) with a concentration of 10 mg/ml. Prior to imaging, the tissues were rinsed with fresh saline solution and set at rest for 5 min in order to avoid fluid flow transients in the specimen during imaging.

3.2.2 Imaging system

The MM-OCE imaging system was previously described in detail [52]. In brief, a titanium:sapphire laser (KMLabs, Boulder, CO) with a center wavelength of 800 nm and a bandwidth of 120 nm provided the probing light for a spectral-domain OCT system. The average power incident on the specimens was 10 mW. The axial resolution was 1.7 μm and the transverse resolution was 16 μm in the specimens, assuming an average tissue index of refraction of 1.4. A small, custom-built, computer-controlled solenoid coil situated 2 mm above the specimen provided the switchable magnetic field for triggering the motion of the MNPs. The strength of the magnetic delivered by the coil was approximately 400 Gauss. Fig. 2.1 shows a schematic of the optical system that includes the solenoid coil.

3.2.3 Data acquisition

Microrheology measurements were made from M-mode imaging data acquired at camera line rates of 5 kHz and 20 kHz to allow high time-resolution displacement measurements of the initial dynamic response of the tissues, as well as longer time measurements that would show the mechanical behavior of the tissue past the initial perturbation. Measurements were made from four different locations close to the center of each specimen. Each M-mode image consisted of 10,000 axial lines and captured 4 cycles of a constant step magnetic field [52]. The phase content of the acquired signals was also used to determine the displacements occurring in the tissue specimens, as previously demonstrated [52]. The displacement sensitivity of the system was 11 nm, allowing us to detect very small displacements in real time and with high resolution. As shown previously, this approach to displacement measurements is preferable to amplitude measurements, whose displacement sensitivity is much lower, on the order of 1 μm [52].

3.2.4 Data analysis

The normalized displacement data was analyzed in Matlab to extract the following biomechanical parameters of interest: the natural frequency of oscillation from the underdamped oscillations, the rise time, defined as the interval between the magnetic field being switched on and the moment the tissue reached the first peak of the oscillation, and the exponential creep term of the displacement following the initial oscillation.

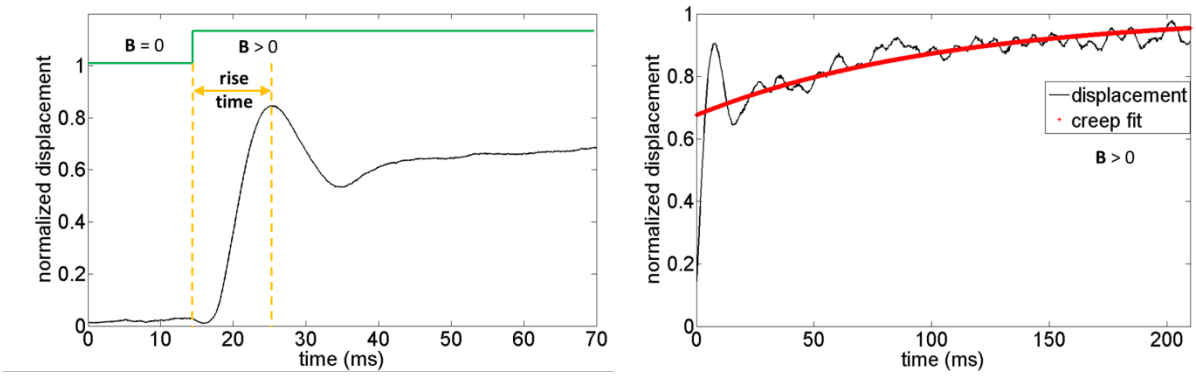

Figure 3.1. Representative lung tissue response. (Left) The displacement data acquired with a 20 kHz camera line rate contains a fast underdamped oscillation from which the rise time is calculated. The natural frequency of the tissue can be calculated by fitting the data after the creep component is subtracted. (Right) The displacement data acquired with a 5 kHz camera line rate is fitted to determine the creep parameter, which describes how fast the tissue displaces over a large time scale compared to the initial oscillation.

Fig. 3.1 shows representative data for lung tissue and highlights the relevant features of the signals that are utilized to calculate the above parameters. The 20 kHz data describes the fast response of the tissue and the 5 kHz data characterizes the slow response. In order to quantify the description of these regimes, the 20 kHz data is fitted to the equation

$$y = A*\sin\left(2\pi ft+\theta\right)*e^{-bt}, \tag{3.1}$$

where y is the displacement, A is the amplitude of the oscillation, f is the natural frequency of oscillation, t is time, θ is a phase factor, and b is the damping parameter. The creep parameter c is calculated from fitting the 5 kHz data to the equation

$$y = 1-a*e^{ct}, \tag{3.2}$$

where a is the amplitude factor.

The Young's moduli of the tissue specimens were calculated based on a Voigt model [77]. In brief, the Young's modulus E is given by the equation

$$E = k\frac{L}{S}, \tag{3.3}$$

where k is the elastic constant of the tissue specimen, L is the height of the tissue, and S is the cross-sectional area of the specimen. k is calculated from the expression

$$k = \left((2\pi f)^2 + b^2\right) * m, \tag{3.4}$$

where m is the mass of the tissue specimen.

3.3 Results and discussion

The tissues measured with MM-OCE contained MNPs that had diffused into the specimens while being immersed in a concentrated suspension of MNPs in saline. Similar to the previous study with silicone tissue phantoms [52], the MNPs likely bind to the extracellular matrix of the tissue, or perhaps are internalized into some cells, and provide access to interrogate the biomechanical microenvironment of the tissue specimens when perturbed with an external magnetic field. I chose to utilize a magnetic field applied in the form of a step function that would be kept on for a period of time sufficiently long so as to allow the observation of the dynamic response of the tissue specimen immediately after the MNPs are set in motion by a rapid-onset then constant magnetic force.

In a preliminary set of experiments, several types of rabbit tissues (adipose, heart, kidney, muscle, lung, and liver) were harvested and MM-OCE was performed. The displacement

data for this set of tissue specimens are shown in Fig. 3.2. It is evident that each type of tissue has a distinctive response. I chose to study the lung and muscle tissues in more depth because they illustrate distinctly different types of responses, appeared more uniform than the other types of tissue, and could be handled more easily, so that each could be sectioned into simple geometric shapes such as cubes. This is important because the boundary conditions can influence the measurements of the natural frequency of oscillation, based on which the Young's moduli are calculated [31, 77].

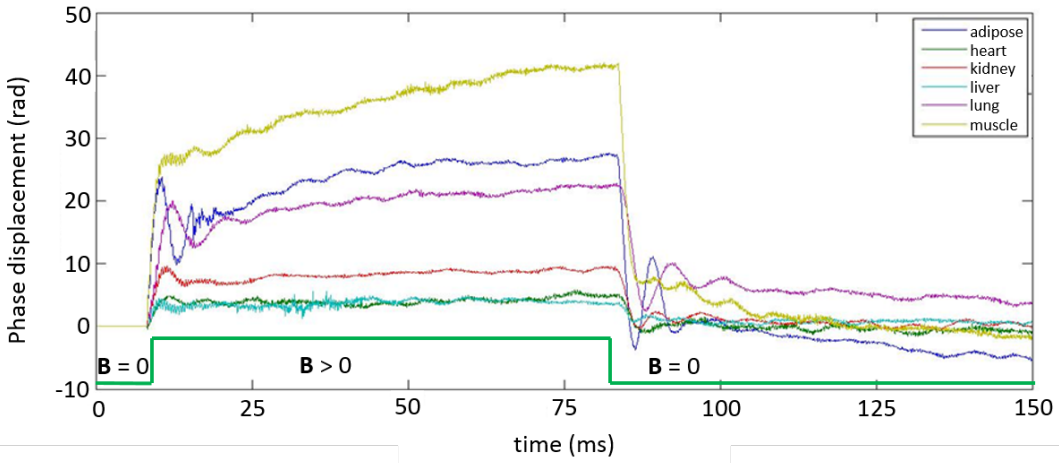

Figure 3.2 Representative MM-OCE signals for different types of rabbit tissues. The first transition corresponds to switch the B field from off to on, while the second one corresponds to switching the field from on to off.

Magnetomotive OCT images (Figs. 3.3 and 3.4 (top)) of rabbit lung and muscle tissues acquired from the center of the specimens show the presence of the MNPs, as demonstrated by the green channel signal. M-mode MM-OCE data was taken at four nearby locations in each specimen and the displacements from bright scatterers along the depth of the axial scans were calculated from the phase data [52]. Depending on the

tissue specimen and location, the number of bright scatterers varied from 6 to 20. The displacement data from these scatterers was averaged and utilized for post-processing. Figs. 3.3 and 3.4 (center) shows two representative MM-OCE signals (normalized displacements) from the lung and muscle specimens. Figs. 3.3 and 3.4 (bottom) shows the noise-level signals from the same specimens when no magnetic field was present. Similar noise-level signals were observed in tissue specimens without MNPs, both with and without the switched magnetic field (data not shown). The noise fluctuations of the displacement are extremely small, compared to the signals recorded when the magnetic field is switched from off to on or vice versa, with a ratio of maximum displacement to noise level displacement of at least 100:1.

Table 3.1 summarizes the averaged values of the natural frequency of oscillation from the underdamped oscillations, the rise time, the exponential creep term of the displacement following the initial oscillation, and the Young's modulus. The natural frequencies of oscillation are comparable to values measured previously in rat lung and muscle [80]. The Young's modulus values are also consistent with previous measurements, though it is to be noted that there is an acknowledged wide range of values in the literature, due to biological variability, physical constraints, chemical environment, and the geometry of the samples [32, 80].

In the previous study with silicone tissue phantoms, the displacements observed contained an underdamped oscillation followed by an equilibrium position [52]. Several cycles of the oscillation were present for these highly homogeneous samples. The more

heterogeneous rabbit lung and muscle tissues exhibit a similar trend in that an underdamped oscillation is also present in their response. However, the damping in these tissue specimens is much faster than in tissue phantoms as only one (in the case of lung) or less (in the case of muscle) cycle of oscillation is observed. Moreover, the tissues undergo creep, as opposed to rapidly settling at an equilibrium position. It is apparent that muscle experiences a steeper creep than lung, while the amplitude of its underdamped oscillation is relatively smaller. Also, when the magnetic field is turned off and the MNPs (and thus the forces on the tissue) are released, the tissue does not revert to its initial position, and some residual strain is present, more so in muscle than in lung.

In conclusion, I have demonstrated the application of MM-OCE in biological tissues, and how phase-sensitive measurements of the tissue response from an applied external step-function magnetic field can yield several important biomechanical properties of the tissue under investigation. These differences observed demonstrate that the behaviors of different types of tissues carry a unique set of information that results from a multitude of factors, such as the physio-chemical constituents of the tissue, the micro-level bonds in the extracellular matrix, the types of cells that make up the tissue, etc. Future studies will begin to elucidate the dependency of each of these factors in the extracted MM-OCE biomechanical data. As a novel optical elastography technique, MM-OCE provides access to this biomechanical information with high resolution, both spatially and temporally, and with high sensitivity, and is a promising technique for advancing the study of biomechanics on the micro scale.

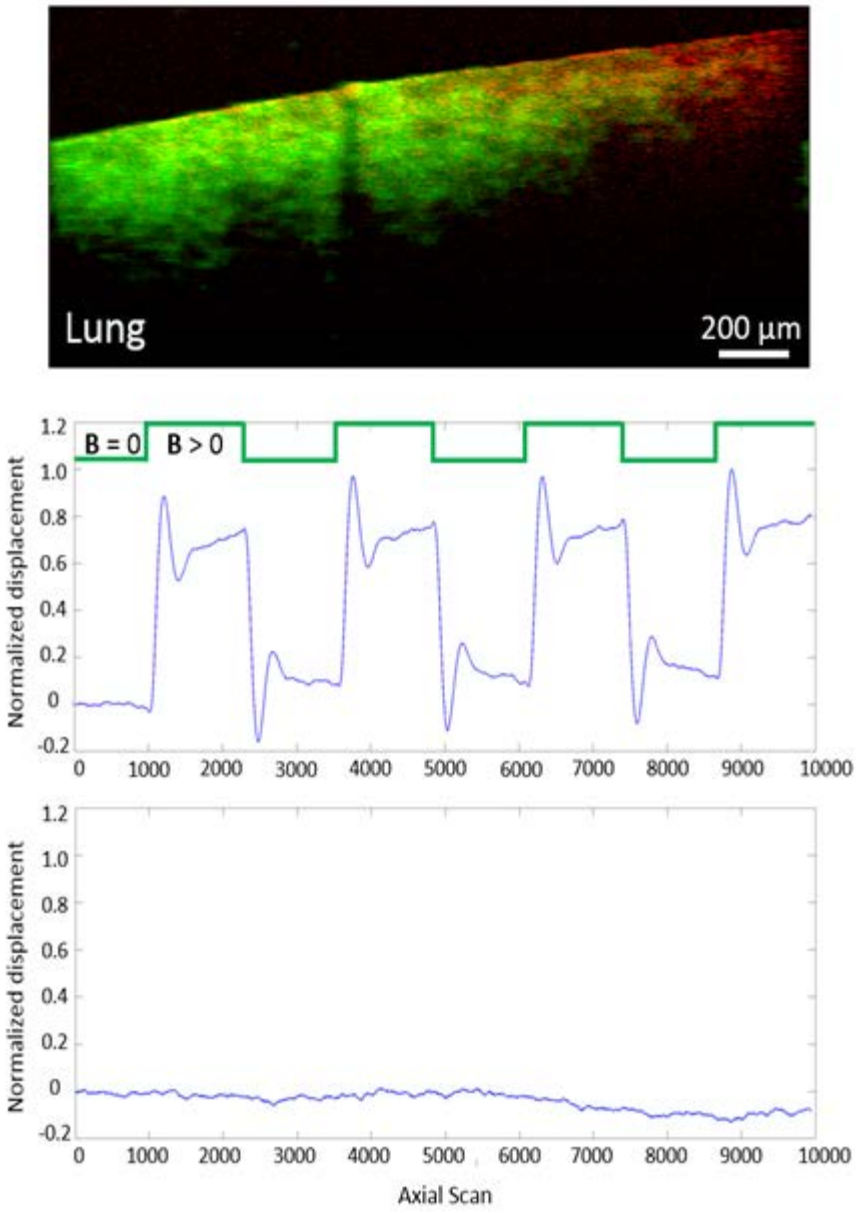

Figure 3.3 MM-OCT and MM-OCE of rabbit lung tissues. (Top) B-mode MM-OCT images of rabbit lung tissues (green channel is MM-OCT signal, red channel is structural OCT signal). (Center) Representative normalized displacements calculated from M-mode phase MM-OCE data taken with a line rate of 20 kHz from rabbit lung while the magnetic field B is modulated as in a step-wise manner (square wave) for 4 cycles (B off followed by B on). (Bottom) Normalized displacement data of lung in the absence of magnetic fields.

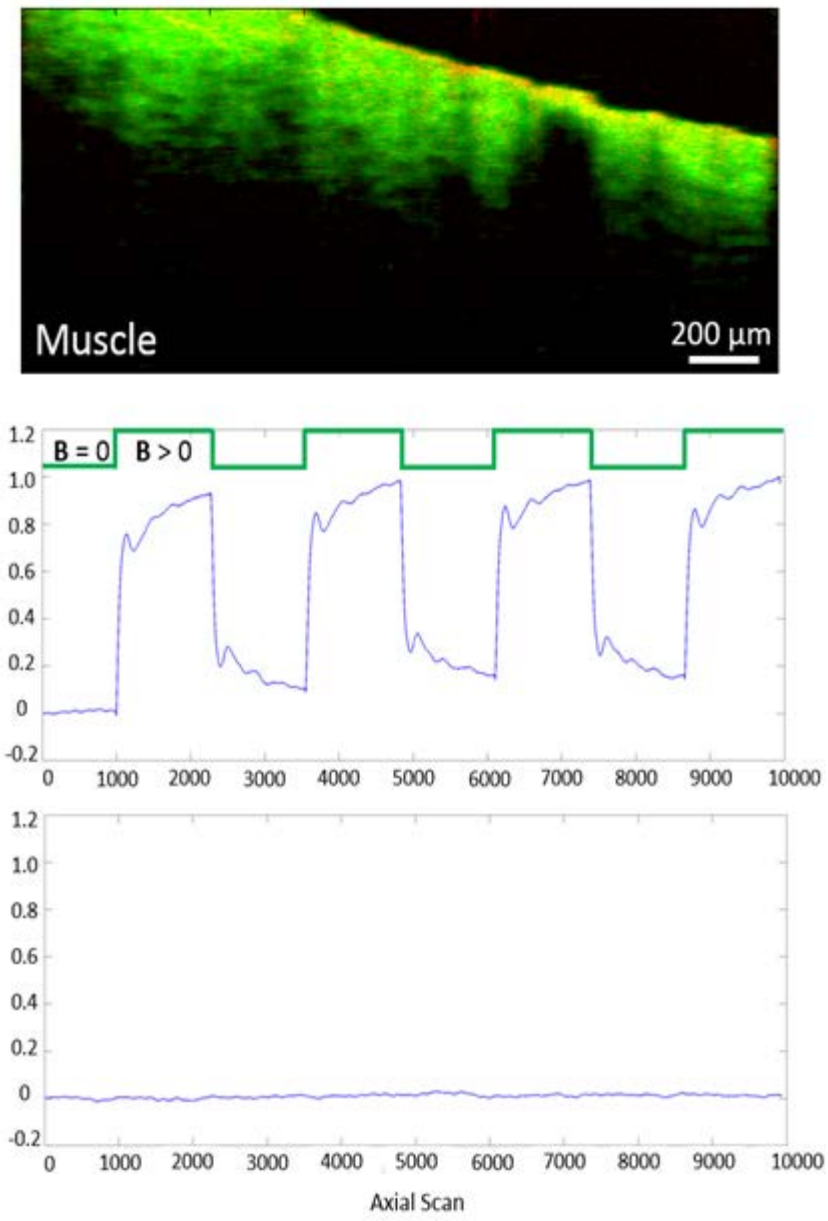

Figure 3.4 MM-OCT and MM-OCE of rabbit muscle tissues. (Top) B-mode MM-OCT images of rabbit muscle tissues (green channel is MM-OCT signal, red channel is structural OCT signal). (Center) Representative normalized displacements calculated from M-mode phase MM-OCE data taken with a line rate of 20 kHz from rabbit muscle while the magnetic field B is modulated as in a step-wise manner (square wave) for 4 cycles (B off followed by B on). (Bottom) Normalized displacement data of muscle in the absence of magnetic fields.

Table 3.1 Biomechanical parameters of rabbit lung and muscle tissue measured with MM-OCE.

Biomechanical Parameter	Muscle	Lung
Creep parameter (1/s)	-8.6 ± 1.9	-6.0 ± 2.4
Rise time (ms)	7.1 ± 0.7	11.3 ± 0.5
Frequency (Hz)	99.6 ± 8.9	57.5 ± 4.7
Young's modulus (kPa)	94.6 ± 15.2	28.5 ± 2.8

4 MAGNETOMOTIVE OPTICAL COHERENCE MICROSCOPY FOR CELLULAR BIOMECHANICS[3]

4.1 Introduction

Cellular mechanics play an important role in normal cell function, and numerous processes at the cellular level result in changes in the elastic properties of different cell components, along with biochemical changes [81-84]. Therefore, it is of great interest to develop technologies that enable measurements of these dynamic mechanical changes, as they would offer new fundamental insight into the inner workings of cells, and further our understanding of both normal and pathological processes. These biomechanical measurements at the cellular level have the potential to lead to new diagnostic paradigms or biomarkers for detecting and treating disease.

In general, cellular elastography techniques can be categorized into active and passive rheology, based on the excitation method employed. In passive rheology, the intrinsic movement of particles internalized by cells or of cellular components is utilized, whereas in active rheology methods, external forces, such as magnetic or optical forces, are used for measuring the cellular mechanical properties. In active rheology, magnetic particles have been widely utilized for measuring cellular mechanical properties. Predominantly, larger sized (several microns) magnetic particles have been used for rheology purposes, as these particles can generate larger magnetic forces (proportional to R^3, where R is the radius of a particle) and their motion can be easily tracked using light microscopy. In magnetic twisting cytometry (MTC), a high magnetic field strength is initially applied to

[3] Crecea V, Graf BW, Kim T, Popescu G, Boppart SA. High-resolution phase-sensitive magnetomotive optical coherence microscopy for tracking manetic microbeads and cellular mechanics. IEEE J Sel Topics Quantum Electronics – Biophotonics, 20:6800907, 2013.

magnetize the ferromagnetic beads and, once the beads are magnetized, a comparatively smaller magnetic field strength is used to impart a torque on the particles, which results in a rotational motion [11]. This technique has been extended by applying oscillating forces [12] and orienting the magnetic fields in different directions, enabling three-dimensional MTC [13].

In another class of techniques termed as magnetic tweezers, a magnetic field gradient is applied under which the magnetic beads undergo predominantly translational motion in the direction of the magnetic field gradient. Magnetic tweezers have been used to measure the local viscoelastic properties of cells [14]. Magnetic tweezers are also a well-established platform for probing at the single-molecule level (particularly for DNA measurements) [85], and can also be implemented in the study of cell functions and processes [86-88]. While the use of magnetic tweezers is preferred for ease of use and robustness, magnetic tweezers suffer from limitations in time resolution and spatial resolution, inherent in the imaging systems utilized to monitor their motion [5]. White-light bright-field video microscopy is the widely used imaging technique in magnetic tweezer studies. However, its main drawback is the fact that it can only measure a 2D plane in real time, while inference of displacement in the third dimension is usually done in post-processing and suffers from lower precision and resolution compared to real-time data [85].

All these techniques employ some form of an imaging method to measure the displacement of the particles. Wide field microscopy techniques measure the

displacements that are within the imaging plane and cannot measure out of plane movements, while techniques such as spectral domain phase microscopy [15] or optical coherence microscopy are only sensitive to the axial displacements [16].

Once the displacements are quantified, a physical model needs to be employed that relates the displacement to the viscoelastic properties. One of the most widely used relationships, especially in passive rheology techniques, are the Stokes-Einstein equations. The particles (can be nanoparticles), once inside the cell cytoskeleton, undergo random fluctuations due to Brownian motion. The mean square displacements (MSD) of these movements are then measured and the generalized Stokes-Einstein equations, which relate the MSD to the viscoelastic properties, are subsequently utilized to extract the viscoelastic parameters of the surrounding microenvironment [17]. Another common method used extensively in the cell mechanics literature is measuring the displacement of the particles under a constant static force applied for several seconds. Due to the viscoelastic nature of the cytoskeleton, the particles undergo a creep response that can be fitted to a number of mechanical models to extract the viscoelastic properties.

In the previous chapters, I have shown that MM-OCE can accurately measure the natural resonant frequencies of silicone samples that mimic the opto-mechanical properties of tissue [52]; however, acquiring magnetomotive signals from single cells presents new challenges, and many investigative opportunities. The current goal is to explore the potential of our imaging system for measuring real-time cellular-level mechanics, which would potentially reveal mechanisms of important cell functions and processes.

I propose a new real-time, multimodal optical imaging technique that incorporates phase-sensitive MM-OCE with optical coherence microscopy (OCM). In OCM the numerical aperture of the imaging objective is higher than in OCT, allowing for higher resolution imaging, on the order of 1 μm [89-91]. Raster scanning of thin biological samples, such as cells, enables two-dimensional imaging. This technique provides fast high-resolution imaging of dynamic mechanical changes in cells probed with magnetic microbeads, which are similarly used in magnetic tweezer studies. This technique has the potential to greatly improve the existing methodology and enable new investigative studies in cellular biomechanics.

4.2 Methods

4.2.1 Cell sample preparation

Three types of cells were probed in this study: mouse macrophages, cell line TIB-67 (J774A.1, ATCC), human breast epithelial primary ductal carcinoma cells, cell line CRL-2314 (HCC38, ATCC), and healthy human breast epithelial cells, cell line CRL-4010 (hTERT-HME1, ATCC). In the experiments using mouse macrophages, two types of magnetic microparticles were utilized. The first type was multifunctional microspheres custom-fabricated in our lab, which have an average diameter and standard deviation of 2.2±1.3 μm. These microspheres consist of a liquid core containing a suspension of iron oxide nanoparticles in vegetable oil, and an encapsulating albumin protein shell [92]. These microspheres have previously been shown to provide good

magnetomotive imaging contrast for OCT [92]. The second type of magnetic microparticles/microtransducers was fluorescent magnetic microbeads (ME04F /9486, Bang Labs, Fishers, IN), with a diameter between 1-2 μm. These magnetic particles consist of iron oxide nanoparticles and a fluorescent dye embedded in a polystyrene matrix that allows for additional co-registered MPM imaging.

In an experiment involving cancer and normal human breast cells, magnetic microbeads (3 μm diameter, Invitrogen Dynabeads®) composed of iron oxide nanoparticles in a polystyrene matrix were used. These magnetic microbeads were either left uncoated or were functionalized with an RGD ligand to target the alpha-v-beta-3 integrin receptors overexpressed on cancer cells.

To facilitate targeting of the magnetic particles/beads to the cells, cultures of each cell type were incubated with magnetic microbeads for a period of four hours at room temperature in a 5% CO_2 environment. Prior to imaging, cell cultures were washed/rinsed with PBS in order to remove excess loose microbeads.

4.2.2 Imaging system

The imaging platform used for this experiment is an integrated optical coherence (OCM) and multiphoton microscope (MPM) [89, 91, 93]. OCM is a high resolution variation of optical coherence tomography (OCT) that uses a high numerical aperture (NA) beam to achieve high lateral spatial resolution. The high NA also restricts the depth-of-field so images are typically acquired in an *en face* orientation, similar to confocal microscopy.

Unlike a confocal microscope that relies only on spatial filtering, OCM produces optical sections of samples using coherence gating in addition to the confocal gating from the high NA. Images are based on optical scattering, which allows the microstructural features of cells or tissue to be visualized. MPM is a nonlinear imaging technique that can be used to excite two-photon fluorescence within the focal volume of a high NA beam. In this study, MPM was used to image multifunctional fluorescent and magnetic microspheres. The integrated OCM-MPM microscope allows simultaneous co-registered imaging with both modalities [36]. This allows the microspheres to be visualized and their location within the cells to be determined. For this study, a small, custom-fabricated magnetic solenoid was integrated below the sample plate to induce an alternating magnetomotive force on the magnetic beads in the cells. The magnetic field strength at the location of the sample was ~400 Gauss, with a gradient of ~10 T/m. The modulation frequency of the coil was 5 Hz.

A schematic of the microscope is shown in Fig. 4.1(A). A dual spectrum laser source is implemented by splitting the output of a tunable Ti-sapphire laser into two beams, one for OCM and one for MPM. The details of this laser source have been previously described [93].

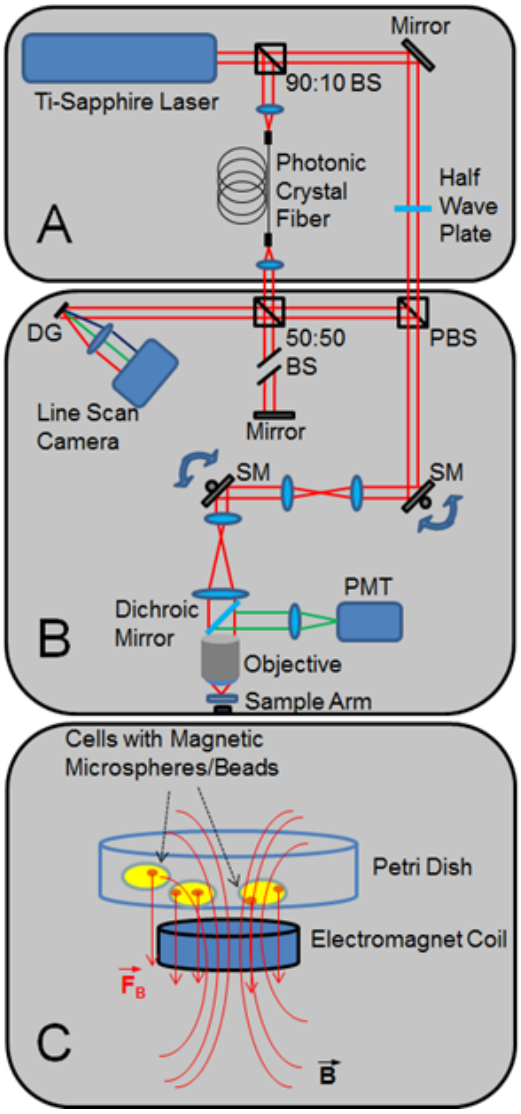

Figure 4.1 Schematic of integrated optical coherence and multiphoton microscope. (A) Dual-spectrum optical source. (B) Sample arm. The red beam lines represent light coming from the laser source as well as light backscattered from the sample, while the green beam lines represent the two photon-excited fluorescence. (C) Zoomed-in region showing the focused sample arm beam with the electromagnet coil, and the field lines generated at the culture of cells containing magnetic microbeads. Abbreviations: BS, beam splitter; DG, diffraction grating; PBS, polarizing beam splitter; SM, galvanometer scanning mirror).

Briefly, the MPM beam is used directly for two-photon excited fluorescence, while the OCM beam is first coupled into a photonic crystal fiber (LMA-5, crystal fiber), where the

spectrum is broadened through supercontinuum generation. The beams are recombined in the sample arm of the interferometer using a polarizing beam splitter. This laser source enables tuning of the center wavelength of the laser to optimally excite fluorescence in MPM while maintaining a broad spectrum for enhanced optical sectioning in OCM. The interference pattern between scattered light in the sample arm and the reference beam is detected by a linescan charge-coupled device (CCD) camera operating at a linescan rate of 33 kHz. OCM processing consists of computational dispersion correction [91] and correction of coherence gate curvature [89] caused by scanning of the beam.

A diagram of the sample arm is shown in Fig. 4.1(B). The dual spectrum laser beam passes through a pair of scanning galvanometers before entering a beam-expanding telescope. The beam is then focused by a 0.95 NA water immersion objective lens (XLUPLFL20XW, Olympus) onto the sample providing a transverse resolution of 2 μm [90]. Fluorescence generated at the focal volume is reflected by a dichroic mirror and focused onto a PMT. Scattered light collected by the objective lens travels back along the beam path to the interferometer. The electromagnet situated below the sample is used to modulate the magnetic microspheres. Axial displacement of the particles and the cell are detected as phase shifts in the OCM signal, as a means for detecting the sample magnetomotive response. The phase sensitivity, determined from the standard deviation of the signal measured from a fixed mirror, was 290 mrad, corresponding to a displacement sensitivity of 13 nm. The amplitude and phase of the oscillations relative to

the driving waveform are determined by the local mechanical environment of the magnetic transducers.

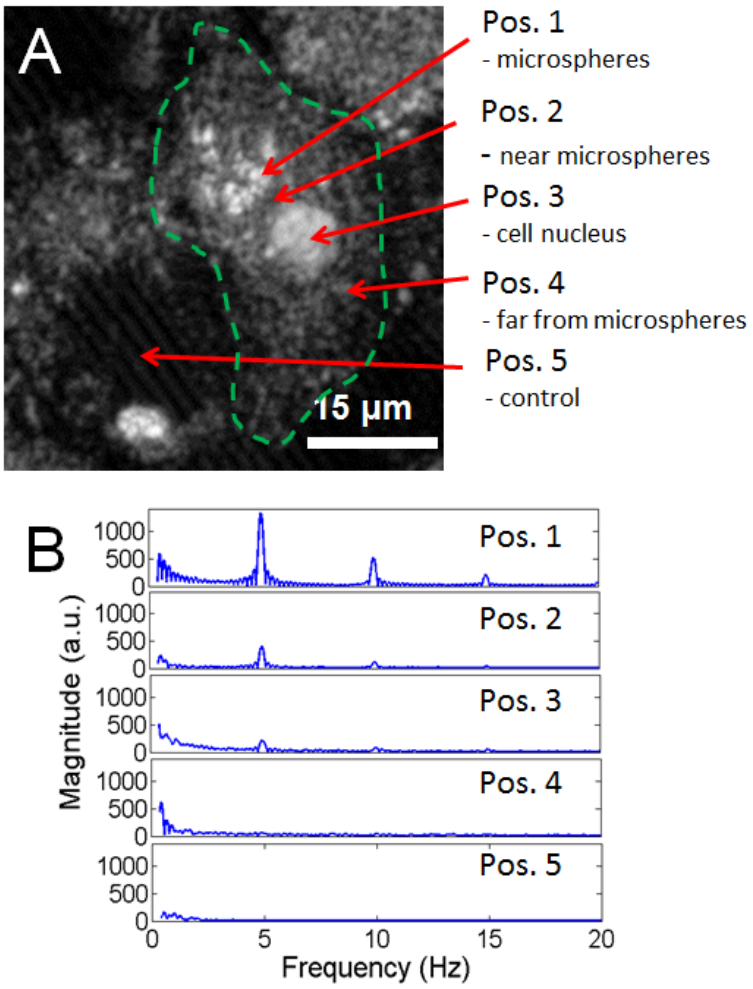

Figure 4.2 Phase-resolved MM-OCE from a single macrophage with phagocytosed microspheres. (A) OCM image of a single macrophage. Arrows indicate locations where M-mode magnetomotive measurements were made in and around the cell (dotted line approximates the contour of the cell). Protein-shell microspheres with a core suspension of magnetic nanoparticles in oil were custom-made in our lab for this experiment. (B) Frequency spectra of the cell displacement data show a response at the magnetic field modulation frequency, 5 Hz, as well as at weaker harmonic modes at 10 Hz and 15 Hz. Positions correspond to those indicated in (A) M-mode signal strength was strongest at the cluster of microspheres.

4.3 Results of magnetic microspheres study

In the first set of experiments, mouse macrophages engulfed the magnetic microspheres that were produced in our lab. Fig. 4.2 shows an OCM image of a representative macrophage that has engulfed microspheres, clustered together at position (1), close to the cell nucleus, as indicated in the figure. The modulation frequency of the magnetic field was 5 Hz, and M-mode OCM data was acquired while the magnetic field was being modulated. Spectral analysis of the displacements measured at the cluster of microspheres, in their immediate vicinity, at the nucleus, away from the cluster of microspheres but still inside the cell, and outside the cell, shows that the signal is strongest at the location of the microspheres and decreases gradually as different locations further away from them are probed. The phase amplitude data for positions (1), (2), and (3) were 10 rad, 5 rad, and 2 rad, respectively, corresponding to displacements of 448 nm, 224 nm, and 90 nm. Positions (4) and (5) did not show a response to the magnetic field. This is to be expected and confirms the fact that the microspheres are the source for the mechanical dynamics measured in and around the cell. The spectral data also show the presence of harmonics of the main 5 Hz mode, with a lower intensity compared to the former. The cell response decreases with increasing distance from the microspheres, and clearly indicates that the measured signal is localized and not a bulk sample response. Validation measurements taken with diffraction phase microscopy [94] and transmission electron microscopy (TEM), shown in Fig. 4.3, confirm that the microspheres were engulfed by the macrophages.

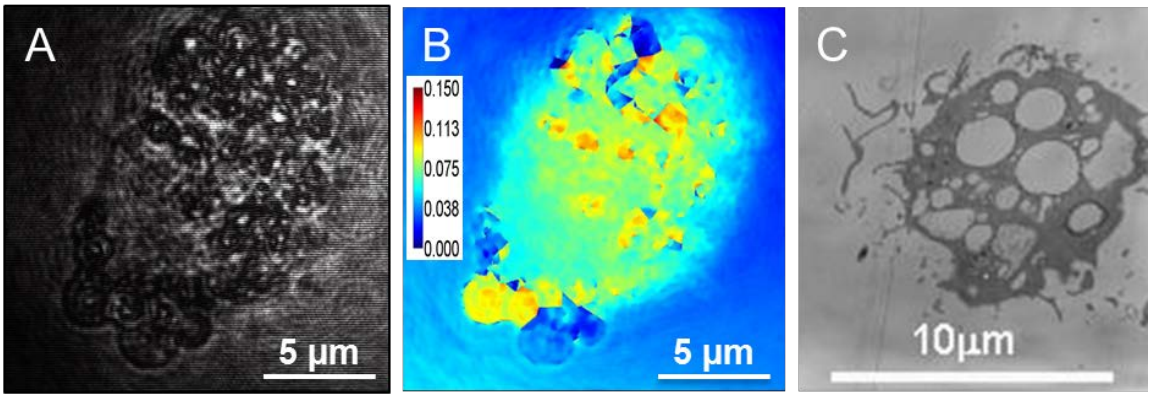

Figure 4.3 Validation of magnetomotive microspheres engulfed by macrophages. (A) Diffraction phase microscopy image of a macrophage exposed to magnetic microspheres, showing phagocytic inclusions of microspheres. (B) Spatial map of phase variance from a video-sequence of diffraction phase microscopy images collected during modulation of an applied magnetic field. Regions of high variance correspond to locations of microspheres. Color bar units are radians. (C) Transmission electron microscopy image of macrophages with engulfed microspheres.

In a second experiment, mouse macrophages engulfed fluorescent magnetic microbeads (Bang Labs). Fig. 4.4 shows a fluorescence image of a pair of microbeads overlaid on the OCM image of a macrophage containing the microbeads. This image data illustrates one advantage of this multimodal optical imaging system, where co-registered images can be used to identify where fluorescently-labeled particles are spatially localized within cells that are structurally imaged with OCM. The dynamic nanometer-scale displacement of the microbeads and cell at the location corresponding to the microbeads is also shown in Fig. 4.4. The measured displacements are sinusoidal, with the same frequency as that of the magnetic field modulation, 5 Hz, as evident by the spectrum in Fig. 4.4.

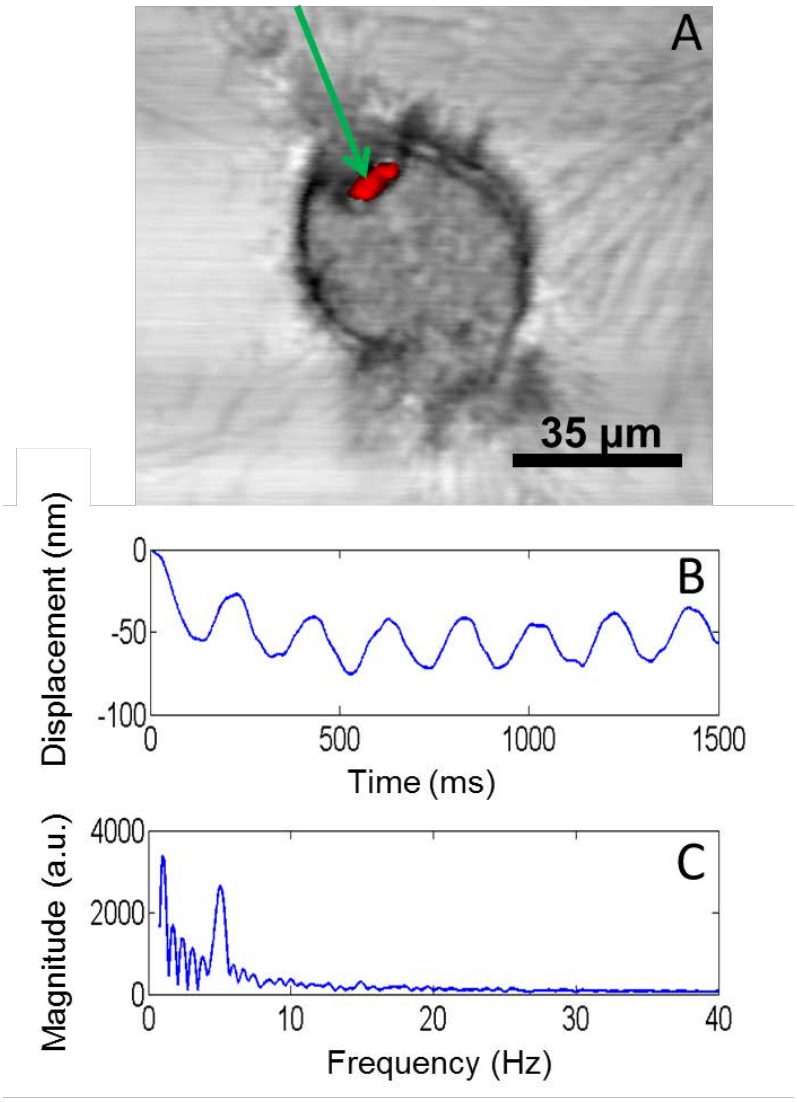

Figure 4.4 Co-registered multimodal imaging and MM-OCE. (A) Simultaneously acquired and co-registered OCM/MPM images of a mouse macrophage that has phagocytosed two fluorescent microspheres (Bangs Labs). The OCM image data is shown in grey-scale, while the two-photon excited fluorescence MPM image data is shown in red. The location of the optical beam for recording MM-OCE displacements is indicated by the green arrow. (B) Plot of sinusoidal axial displacement of the microspheres as calculated from phase data. (C) Frequency spectrum of the magnetomotive signal obtained by taking the Fourier transform of the displacement signal during 5 Hz modulation by the external magnetic field.

Lastly, cancer and normal human breast epithelial cells were probed with RGD-targeted and non-targeted magnetic Dynabeads. Fig. 4.5 shows bright field microscopy images of the four different combinations of cells and Dynabeads.

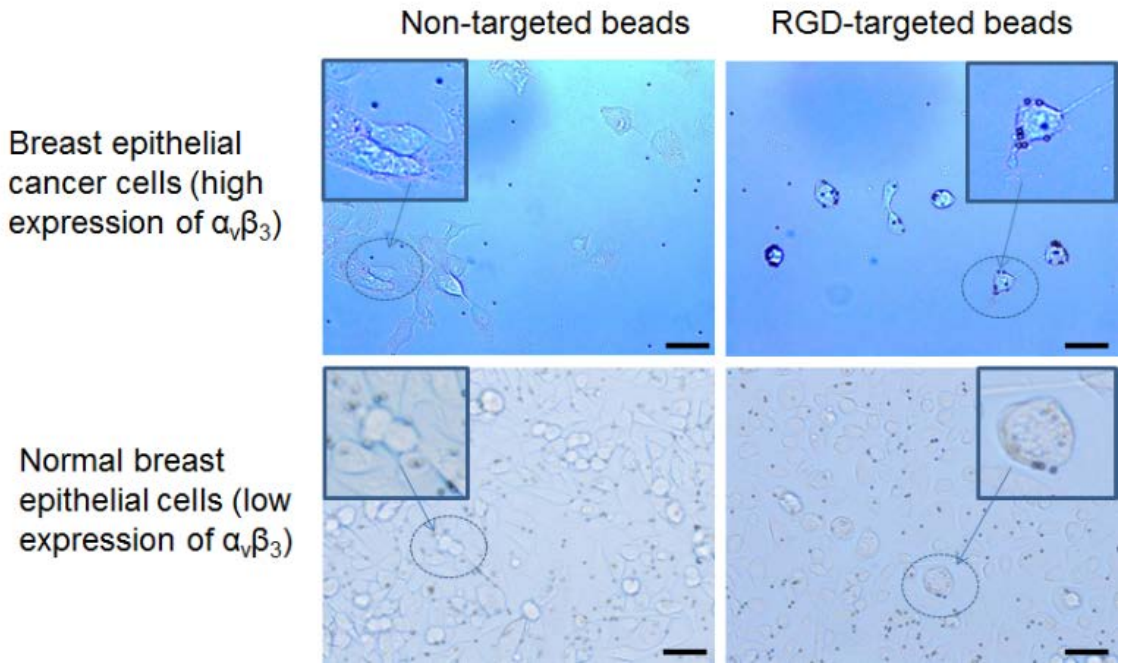

Figure 4.5 Molecular targeting of Dynabeads for MM-OCE measurements. Bright field microscopy images of cell cultures (human breast epithelial and primary ductal carcinoma cells) that were incubated with targeted and non-targeted magnetic Dynabeads (dark point-like objects). The targeted beads show preferential attachment to the cancer cells that over-express the alpha-v-beta-3 integrin receptor. Inset images are zoomed-in regions to highlight the spatial location of the Dynabeads relative to the cells. Scale bar indicates 25 μm.

It is evident that the targeted beads attach strongly to the cancer cells, and less so to the normal cells, while the non-targeted beads do not adhere in any predictable or preferential manner to either of the two cell lines. In these experiments, the magnetomotive signals were weaker than in previous experiments, with less than 20% of the Dynabeads that attached to cells responding to the magnetic field. Video data captured by instantaneous

spatial light interference microscopy (iSLIM) [95], a quantitative phase imaging technique, of cancer cells with targeted Dynabeads show only two out of sixteen Dynabeads in the field of view responding to the magnetic field modulation. A representative image of the signal standard deviation in time of the cell culture and Dynabeads is shown in Fig. 4.6.

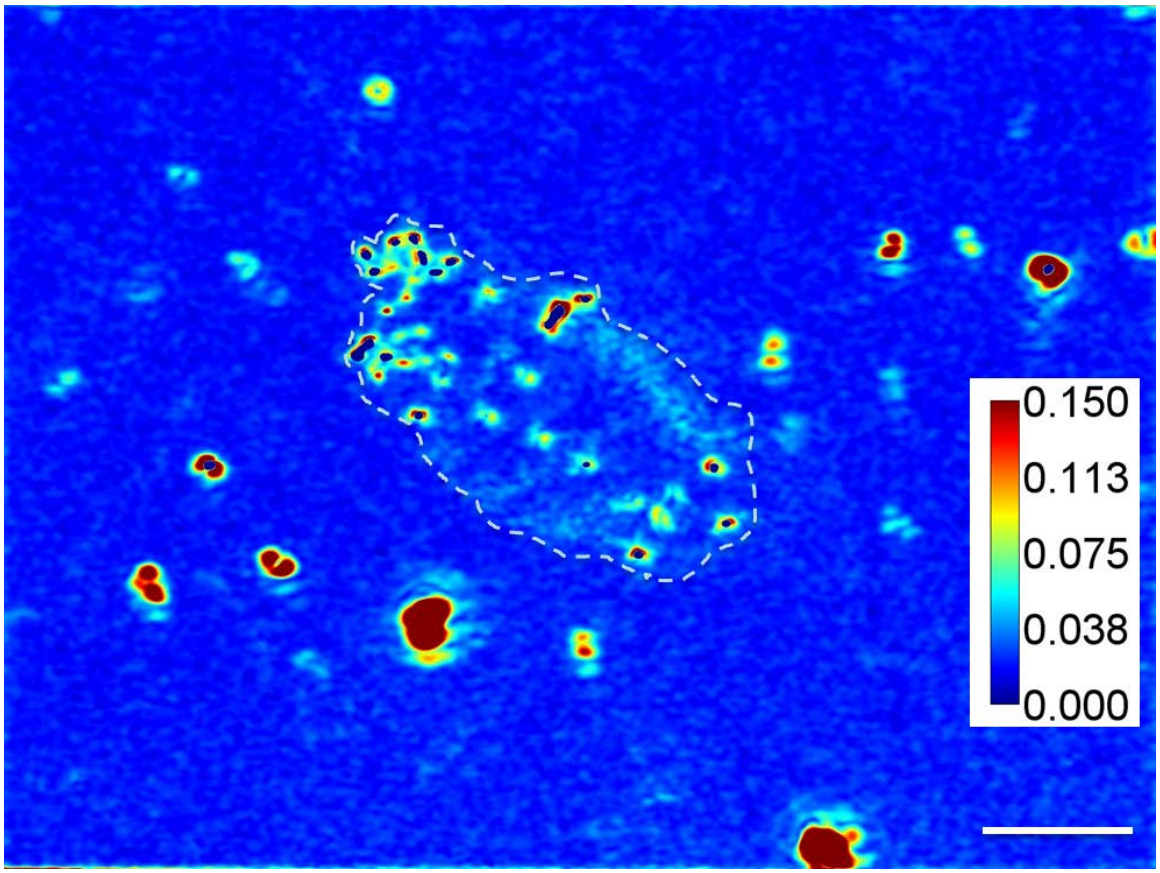

Figure 4.6 Validation of magnetic Dynabead response from cancer cells. Instantaneous spatial light interference microscopy (iSLIM) image of cancer cells with targeted Dynabeads show high standard deviations in time at the location of the Dynabeads. The data were taken using iSLIM with a 40x/0.75NA objective. The time lapse was taken at 13 Hz for two seconds, and then processed to map the standard deviation of each pixel. The red and blue colors indicate areas with high and low standard deviations of the optical path length, respectively. Scale bar indicates 30 μm. Color bar units are radians. Dotted line approximates the contour of the cell.

High values are registered at the location of the beads. No significant differences in magnetomotive signal amplitude or oscillation patterns were observed between the cancer cells with targeted Dynabeads and the normal cells with targeted Dynabeads, suggesting that the biomechanical properties of the targeted alpha-v-beta-3 integrin receptors are likely similar. The cell cultures containing non-targeted beads that attached non-specifically to some of the cells also produced magnetomotive signals from a low percentage of cells. Fig. 4.7 is representative of some relative displacements and frequency spectra of the magnetomotive signals from three neighboring non-targeted Dynabeads attached to cancer cells. It is evident that bead number 3 does not produce a signal, while beads 2 and 3 do. These different displacements oscillation patterns, and in some cases, no displacement, highlight the observed variability.

4.4 Cellular biomechanics utilizing magnetic nanoparticles

I have also explored the possibility of employing MNPs for cellular biomechanics. MNPs can offer significant advantages for measuring the cellular biomechanics. Over the years, several studies have been conducted by research groups to systematically evaluate the cellular uptake of MNPs. The cellular uptake of the MNPs depends on a number of factors such as the types of cells, the nature and surface-coating of the particles, the concentration and duration of the incubation period, etc. Prussian blue staining or electron microscopy (e.g. TEM) have been typically used to evaluate the uptake of MNPs by the cells [96]. In one study, six different mammalian cell lines were incubated with Dextran coated MNPs for 48 hours at different concentrations. As expected, the cellular uptake was different for different cell lines, and increased with

increasing concentration of MNPs. At an MNP concentration of 100 ug/ml, the iron content in the different cell lines varied from approximately 2 pg/cell to 9 pg/cell [96]. In addition to the concentration, the surface coating on the MNPs can also significantly affect the cellular uptake. The surface of the MNPs used for biological studies is chemically coated with a biocompatible material to increase their circulation time and reduce their toxicity. In one study, the MNPs coated with PEG had a significant higher uptake in cancer cells (113 pg/cell after 4 days) compared to macrophages,[97] while in another study the uptake of MNPs in hepatocytes increased to as high as 743 pg/cell after surface coating with lactobionic acid [98]. All these studies suggest that there is a great variability in the amount of cellular uptake of MNPs, and that it would depend on numerous factors and experimental conditions.

Magnetic particles within the cytoplasm experience several competing forces arising due to viscous drag, random Brownian forces, and magnetic forces. The size of the magnetic particles strongly influences which forces dominate, as these forces scale differently with the size of the particle. The magnetic force on a particle of radius R scales by R^3, the viscous drag force by R_h (the hydrodynamic radius), while the Brownian displacement is proportional to $R_h^{-1/2}$ [99]. This suggests that smaller particles will have larger random steps (due to Brownian motion), while they would also be more difficult to manipulate in a controlled manner. However, it is to be noted that although manipulating individual nanoparticles might be challenging, controlling clusters or aggregates of MNPs can be technically feasible. Several studies have shown that when a magnetic field is applied to

MNPs, these tend to aggregate and the magnetic dipole-dipole interactions become dominant, moving the aggregates/clusters along the magnetic field gradients [100].

Table 4.1 shows some typical values reported in literature of the forces experienced by different sized particles under a magnetic field gradient. Typically a force of around 100 pN on a 1 μm size bead is required to cause a displacement of about 100 nm inside the nucleus of the cell [101]. It is also noted that the magnetic field gradients used in these studies are significantly higher (1000 – 8000 T/m) than the magnetic field values of ~ 0.04 Tesla and a gradient of ~ 10 T/m used in the MM-OCM studies presented in this thesis. Using these values (i.e., B = 0.04 T, ∇B = 10 T/m), a 100 nm radius particle will experience a force of 0.004 pN, which is not enough to generate measurable displacement in MM-OCM, and explains the lack of a magnetomotive signal using MNPs in the MM-OCM studies.

Table 4.1 Magnetic forces of varying size magnetic particles under different field gradients

Diameter of particles (nm)	Force (pN)	Magnetic Gradient (T/m)	Reference
350 nm	12	8000 T/m	[102]
4500 nm	130	n.a.	[103]
38 nm	0.015	3000 T/m	[99]
2800 nm	1000	8000 T/m	[101]
100 nm	7	8000 T/m	[101]

In PDMS-phantoms and biological tissues, efforts were made to distribute the MNPs evenly throughout the sample volume, either during the preparation phase (for the PDMS-tissue phantoms), or by soaking the biological tissue in a high concentration MNP solution (10 mg/ml) for several hours (4 – 8 hours), which allowed the diffusion of MNPs within the tissues. The high concentration of particles within the magnetic excitation volume results in a collaborative effect resulting in large measureable displacements in the tissues. On the other hand, the mechanism of MNP bonding to cellular components is based on biochemical interactions at the molecular level. The MNPs can either be functionalized to target specific cellular components and surface receptors, or they can be internalized by the cells. Because these MNPs are either bound to some cell surface receptors or aggregate in the form of vesicles inside the cytoplasm,[96] the cell-based magnetomotion is more localized compared to the bulk response measured in MM-OCE in tissue phantoms. In addition, the MNPs, due to their small size, scatter very little light. The movement of the MNPs is not directly measured in MM-OCE; rather the MNPs, once perturbed, move the adjacent tissue scatterers, which are detected in tissues and phantom-based MM-OCE measurements. In cell-based MM-OCM studies the MNPs might not be adjacent to any highly scattering structures. Hence the signal measured directly from the MNPs inherently has a low SNR, which affects the consistency and reliability of the displacement measurements in cell-based MM-OCM studies.

In MM-OCE measurements of PDMS-phantoms and tissues, the bulk response of the whole sample is measured and the magnetomotive response is characterized by the resonance frequency of the sample. This resonance frequency is dependent not only on

the mechanical properties of the sample, but also on the sample geometry and size. Experiments using phantoms and biological tissues were performed with samples of controlled geometry and dimensions, which allowed the comparison between different sample and tissue types. However, in the MM-OCM experiments on cells, I did not see any resonant frequencies due to the small sizes of cells. Moreover, the lack of control of the dimensions and geometry of the cells limited the ability to perform a meaningful comparison between and across different cell lines. Furthermore, I did not find any evidence in the literature that cells exhibit any mechanical resonances.

4.5 Discussion

I have demonstrated a new real-time multimodal high-resolution imaging technique that combines OCM and MPM with magnetic actuation for dynamic nano-scale magnetomotive displacement measurements at the cellular level. Magnetic microparticles act as transducers by attaching to or being engulfed by cells, thus enabling probing of the molecular receptor or cellular mechanical environment. Microspheres and beads were chosen for this study because single or small aggregates of magnetic nanoparticles were found insufficient to generate a measurable magnetomotive signal, either because the magnetic force generated by our custom solenoid was too small to set a nanoparticle bound to the surrounding cellular medium in motion, or due to the fact that, even if the nanoparticle moved, its displacement would be too small to have a measurable effect.

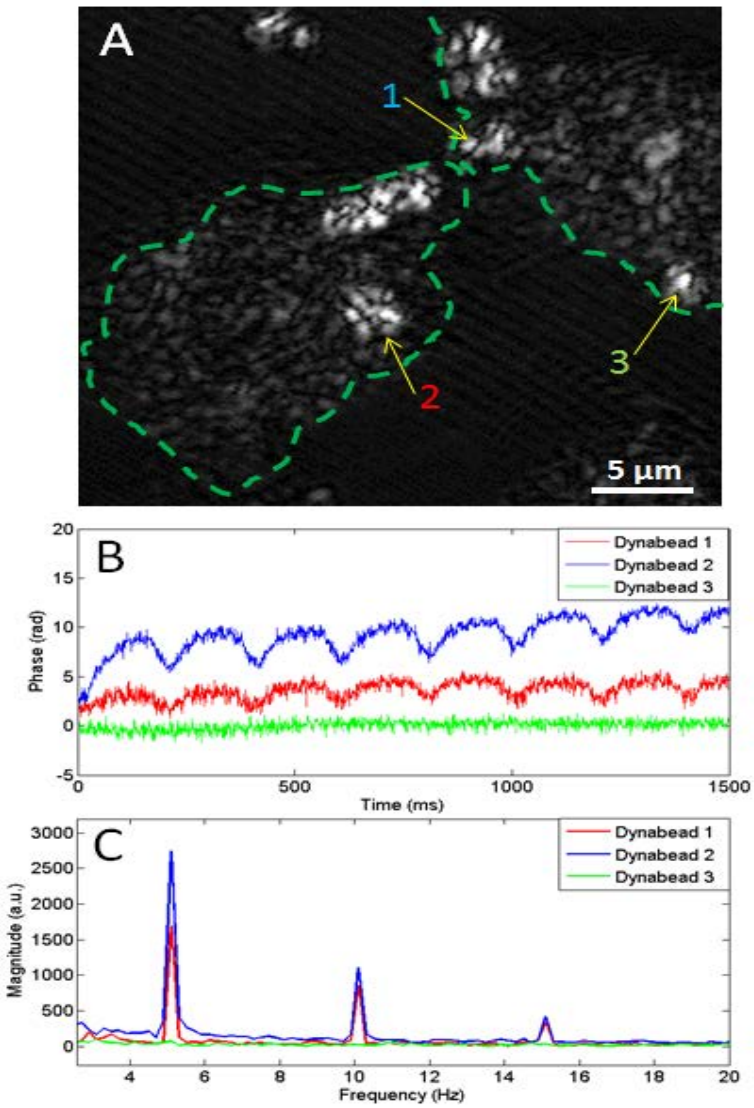

Figure 4.7. Magnetomotive response from cancer cells. (A) Representative OCM image of cancer cells (dotted line approximates cell contours) showing non-targeted Dynabeads (indicated by arrows) attached to the cells. M-mode magnetomotive signal data was taken at locations 1, 2, and 3. (B) Representative phase displacement responses of the cells at the locations of the Dynabeads indicated in part (A). The different amplitudes exemplify the variability of the signals from varying spatial positions on the cells. (C) The frequency spectra (via the Fourier transform) of the displacement signals plotted in (B) during 5 Hz modulation by the external magnetic field.

I initially chose macrophages for the proof-of-principle demonstration of this technique due to their versatile function that ensures phagocytosis of magnetic microspheres and

localization in the interior of the cell. This platform constitutes a reliable model with a well-understood mechanism of microparticle phagocytosis. When probed with an external magnetic field, the microspheres experience a force that sets them in motion, which engages the cellular architecture in a similar dynamic response. The imaging system is capable of detecting this motion with nanometer-scale sensitivity, as shown in Fig. 4.3. Because the cyto-architecture and cellular membrane are elastic, it was expected that the largest displacements would be found at the location of the microspheres, and show gradually less displacement at points further away from the microsphere location. The acquired data confirmed this prediction.

Two-photon excited fluorescence imaging (Fig. 4.4) enhances the structural imaging obtained with OCM by spatially locating the microparticles inside cells with high precision. These results also demonstrate the possibility for more sophisticated, versatile, probing of cell mechanics with an emphasis on certain functional groups, based on specialized dyes that may be employed to reveal specific organelles or processes inside a cell.

This technique is also appropriate for the study of the mechanical responses of molecular membrane-bound receptors on cells, using magnetic agents that are functionalized and targeted to these external membrane receptors, such as the alpha-v-beta-3 integrin receptors found on normal human breast epithelial cells and over-expressed on the human breast cancer cells (Fig. 4.5). However, the measured magnetomotive displacement signals from these experiments were found to be more variable compared to the macrophage experiments. This finding may be due to several different factors, such as

the strength of the molecular bond between the RGD-functionalized magnetic Dynabeads and the outer membrane-expressed integrin receptors of the cell (compared to the phagocytosed microspheres residing inside the macrophages in the first set of experiments), the stiffness of the breast epithelial cell membrane, possibly higher than that of macrophage membrane, and the potential inhomogeneity of the mechanical properties of the biological cell culture microenvironment. The oscillatory displacements patterns observed for the samples of breast cells with the Dynabeads have a rectified profile, different from the sinusoidal-type of displacement measured from macrophages. The difference in the mechanism of binding between the microspheres or beads and the host cell may account for this. Further investigations are needed to elucidate the details of the physical biochemistry at play in these systems. The technique presented here, however, is a novel platform for these future studies.

The inherent variability of the biological samples results in variable signal strengths, a fact previously observed in similar cellular studies that employ magnetic tweezers [85, 86]. However, responsive microspheres are reliable in that repeated measurements under the same conditions render similar magnetomotive signals that are always modulated at the same frequency as the solenoid coil driving frequency. This demonstrates that the technique presented in this chapter is robust and appropriate for studies that would focus on characterizing the biological variability of well-controlled systems, while taking full advantage of the high sensitivity to nanometer-scale displacements. These results will also lead to future research to determine the sources of the variability, which will greatly advance our understanding of cellular processes and support the further development of

novel methodologies for manipulating and interrogating the biomechanical properties of molecules and cells. Other possible applications include drug testing, studies of fundamental metastatic changes in cells, and toxicology studies.

Magnetic tweezers have become an established technique for measuring the mechanical properties of molecules and cells. However, this technique offers limited axial displacement resolution, hampering its use in many applications. The methodology of using phase-sensitive magnetomotive measurements in a multimodal microscope platform presented in this study has the potential for becoming a new paradigm for assessing molecular and cellular biomechanics. The high nanometer-scale sensitivity to axial displacements facilitates access to probing macromolecular bonds and could enable measurements of biomechanical properties at the cellular level. This novel approach for studying cellular processes and functions could offer new insight into how different mechanical processes, such as stretching of membranes or receptors that are attached to controllable magnetic beads, affect them. Rigorous modeling and simulations of cellular and extracellular microenvironments, coupled with statistically significant experimental studies using magnetomotive forces, are further needed to rigorously investigate and spatially map the biomechanical properties of single cells and their associated molecular receptors.

5 CONCLUSIONS AND OUTLOOK

The understanding of biological systems is of great interest for the advancement of basic sciences and medicine, in particular for disease detection and treatment. I have discussed the need for high resolution imaging tools that can capture minute details of biological components ranging from sub-cellular components, macromolecular groups, cells, to microscopic tissue morphology and macroscopic biological structures. Besides taking snapshots of discrete states of this type of systems, the ability to monitor processes taking place within them in real time is also extremely valuable, as it offers insight into the dynamics and mechanisms of biological processes. This can increase our understanding of a multitude of phenomena, such as cell growth or the onset and progression of disease at a cellular or tissue level, to name just a few. Hopefully, researchers can apply this new knowledge and develop new therapies. Understanding nature could help us mimic it or even compete with it in ways that are beneficial to humanity.

To this end, I combined the benefits and versatility of an advanced imaging technique, OCT, with the simple concept of the interaction of MNPs with a magnetic field, to develop a new functional imaging methodology, MM-OCE. Magnetic particles that attach to cells or tissue help us gain access to the biological mechanical environment, which can then be interrogated by applying an external magnetic field that sets the magnetic particles/transducers in motion and solicits a mechanical response from the specimens under study. The displacements of the samples are measured with OCT in real time and with nanometer-scale sensitivity (to be more precise, the sensitivity is 11 nm in the imaging system).

The proof of principle demonstration of MM-OCE involved the fabrication and testing of a set of samples with varying elastic properties. I used silicone phantoms that mimic biological tissue both optically and mechanically, and embedded magnetic nanoparticles throughout their volume. I demonstrated that, when subjected to a constant magnetic force resulting from the step-wise application of an external magnetic field, these samples undergo nano to micro-scale underdamped oscillations that contain information about their resonant frequency and damping constant, parameters characteristic of viscoelastic materials. The linear relationship between the resonant frequency of oscillation and the square root of the Young's modulus of the samples, as predicted by a Kelvin-Voigt model, was confirmed.

For the MM-OCE study of biological tissues I used a rabbit model. In this case, the mechanical response was similar to that observed in the silicone phantoms, but two important distinctions were immediately apparent: the oscillations were damped much faster, indicating larger viscosity, and there was also a creep component, characteristic of biological tissues but not of polymeric materials such as silicone. Muscle tissue has a steeper creep profile and lower amplitude of oscillation. This suggests that each type of tissue has a characteristic behavior, even though there are similarities in the tissues' overall behavior. Future studies should address the distinguishing features in the biomechanical profile of different types of tissues.

I also explored the possibility of implementing MM-OCE concepts in the study of cell biomechanics. I showed that different types of cells can be coupled with multimodal

magnetic microspheres that can be functionalized for targeting of specific cell receptors and that reliable biomechanical signals upon sinusoidal magnetic actuation of the cell-particle bonds can be obtained. However, I also noticed a large variability of the signals collected, and in some cases the magnetic microspheres/beads did not seem to move. It is understandable that cells would have a less uniform behavior than tissues when probed individually, given their lack of homogeneity on the micron scale. Tissues have more of a bulk behavior and are less heterogeneous.

A number of models have been used to describe cellular mechanics; however, it has been widely acknowledged that no single model or theory can explain the intricacies and complexities of the cell mechanical environment, and the selection of an appropriate mechanical model is still a matter of open debate [81]. Standard mechanical models based on parallel and series combinations of springs and dashpots have been extensively employed in the literature. However, recently, power law models [104, 105] or models that fit the creep response to a single or double exponential [106], have been generating considerable interest and have been shown to describe the cellular viscoelastic properties with success [81]. In the MM-OCM cells studies, I decided to apply a sinusoidal excitation with the hypothesis that the amplitude and phase of the magnetomotive response from magnetic particles in different cells lines will vary depending on the elasticity and viscosity of the cell microenvironment respectively. However, I did not see any significant variation in the phase lag between the driving force and the magnetomotive response in the cell samples, and the phase lag was very small in all the experiments. The measurement of the amplitude across different cells or at different bead

locations was also problematic. The amplitude of displacement depends on the amount of magnetomotive force, the binding strength of the magnetic particle to the receptors, etc. However, due to the large variation in the amplitude of the magnetomotive signal, it was difficult to quantitatively relate this to the cell mechanical properties. Future MM-OCM cellular studies can benefit from the following:

a) A coil with a higher magnetic field gradient will be highly desirable for future MM-OCM cellular studies. Several studies have used custom-made coils with a tapered tip that can achieve magnetic field gradients of ~ 8000 T/m.

b) Precise calibration of the magnetomotive force is necessary to quantitatively relate the magnetomotive response to the viscoelastic properties of the cell. This can be done in several ways. One way is by placing magnetic particles (to be used in experiments) with known sizes in a medium with known viscoelastic properties and measuring the displacement of the particle using a standard microscope under the influence of a given magnetic field strength. The distance of the sample from the coil can be changed and a plot of magnetic force against distance can be used for calibration.

c) From the literature it is apparent that the creep response of the particles under a constantly applied force can be a good metric for the viscoelastic properties of the cytoskeleton. In future studies, a static magnetic field can be applied for more than one second. The displacement of the particle as a function of time can be measured with OCM and fitted with power law models or single or double-exponential models to extract the viscoelastic properties.

d) If the magnetomotive force can be precisely calibrated, then techniques similar to MTC with oscillating forces can be utilized [104, 105]. The magnetomotive response over a broad range of frequencies, i.e. 1-300 Hz, can be applied, and the amplitude and phase can be utilized to estimate the viscoelastic parameters.

The possibility of utilizing MNPs for the study of cell biomechanics should be further explored; however, there are several difficulties to overcome. When cells are exposed to MNPs they preferentially attach to a relatively small fraction of them. The forces acting on individual MNPs are on the order of pN, too small for individual MNPs to effect a dynamic mechanical change in the cell. In tissues and tissue phantoms, relatively high concentrations of MNPs can be embedded through the process of diffusion or fabrication. These specimens are more homogenous than cells and have a bulk response to forces within their volume, whereas cells are more heterogeneous and when MNPs are attached to them, a very high local concentration of MNPs is needed for motion to be triggered. It is hard to achieve such high concentrations in live culture cells because there is little control over how they interact with foreign agents, such as MNPs. New study models that address this issue need to be developed.

The main contribution of this thesis is the development of a highly sensitive versatile optical imaging technique that utilizes magnetic nanoparticle-induced motion to map out the elastic properties of biological samples. The feasibility of this approach was both theoretically justified and experimentally verified in tissue-mimicking phantoms, biological tissues, and cells. The inherent variability and complexity in biological tissues

and cells pose some unique challenges in assessing their biomechanical properties. To describe these complexities and variability in tissues and cells, future work should include development of rigorous biomechanical models and should couple these with our experimental technique for a thorough description of the biomechanics of biological specimens.

6 REFERENCES

[1] A. F. Fercher, W. Drexler, C. K. Hitzenberger, and T. Lasser, "Optical coherence tomography - principles and applications," *Rep. Prog. Phys.*, vol. 66, pp. 239-303, 2003.

[2] A. L. Oldenburg, F. J. Toublan, K. S. Suslick, A. Wei, and S. A. Boppart, "Magnetomotive contrast for *in vivo* optical coherence tomography," *Opt. Express*, vol. 13, pp. 6597-6614, 2005.

[3] C. Sun, B. Standish, and V. X. Yang, "Optical coherence elastography: current status and future applications," *J. Biomed. Opt.*, vol. 16, p. 043001, 2011.

[4] F. I. Michael and C. B. Jeffrey, "Tissue motion and elasticity imaging," *Phys. Med. Biol.*, vol. 45, pp. v-vi, 2000.

[5] N. W. Tschoegl, *The phenomenological theory of linear viscoelastic behavior: an introduction*: Springer-Verlag, 1989.

[6] A. Wineman and K. Rajagopal, *Mechanical Response of Polymers*: Cambridge University Press, 2000.

[7] J. Ferry, *Viscoelastic Properties of Polymers* John Wiley and Sons, 1980.

[8] M. Sridhar, J. Liu, and M. F. Insana, "Elasticity imaging of polymeric media," *J. Biomech. Eng.*, vol. 129, pp. 259-72, 2007.

[9] D. Ouis, "Characterization of polymers by means of a standard viscoelastic model and fractional derivate calculus," *Int. J. Polym. Mater. Po*, vol. 53, pp. 633-644, 2004.

[10] J. F. Greenleaf, M. Fatemi, and M. Insana, "Selected methods for imaging elastic properties of biological tissues," *Annu. Rev. of Biomed. Eng.*, vol. 5, pp. 57-78, 2003.

[11] J. Ophir, S. K. Alam, B. Garra, F. Kallel, E. Konofagou, T. Krouskop, C. B. Merritt, R. Righetti, R. Souchon, S. Srinivasan, and T. Varghese, "Elastography: imaging the elastic properties of soft tissues with ultrasound," *J. Med. Ultrason*, vol. 29, pp. 155-171, 2002.

[12] I. Cespedes, J. Ophir, H. Ponnekanti, and N. Maklad, "Elastography: elasticity imaging using ultrasound with application to muscle and breast *in vivo*," *Ultrason. Imaging*, vol. 15, pp. 73-88, 1993.

[13] R. Muthupillai, D. J. Lomas, P. J. Rossman, J. F. Greenleaf, A. Manduca, and R. L. Ehman, "Magnetic resonance elastography by direct visualization of propagating acoustic strain waves," *Science*, vol. 269, pp. 1854-7, Sep 29 1995.

[14] A. Manduca, T. E. Oliphant, M. A. Dresner, J. L. Mahowald, S. A. Kruse, E. Amromin, J. P. Felmlee, J. F. Greenleaf, and R. L. Ehman, "Magnetic resonance elastography: non-invasive mapping of tissue elasticity," *Med. Image Anal*, vol. 5, pp. 237-254, 2001.

[15] A. J. Romano, J. A. Bucaro, R. L. Ehnan, and J. J. Shirron, "Evaluation of a material parameter extraction algorithm using MRI-based displacement measurements," *IEEE Trans. Ultrason. Ferroelectr. Freq. Control*, vol. 47, pp. 1575-1581, 2000.

[16] R. Sinkus, M. Tanter, S. Catheline, J. Lorenzen, C. Kuhl, E. Sondermann, and M. Fink, "Imaging anisotropic and viscous properties of breast tissue by magnetic resonance-elastography," *Magn. Reson. Med*, vol. 53, pp. 372-387, 2005.

[17] O. V. Rudenko, A. P. Sarvazyan, and S. Y. Emelianov, "Acoustic radiation force and streaming induced by focused nonlinear ultrasound in a dissipative medium," *J. Acoust. Soc. Am.*, vol. 99, pp. 2791-2798, 1996.

[18] S. Chen, M. Fatemi, and J. F. Greenleaf, "Remote measurement of material properties from radiation force induced vibration of an embedded sphere," *J. Acoust. Soc. Am.*, vol. 112, pp. 884-889, 2002.

[19] C. Reynaud, F. Sommer, C. Quet, N. El Bounia, and T. M. Duc, "Quantitative determination of Young's modulus on a biphase polymer system using atomic force microscopy," *Surf. Interface Anal*, vol. 30, pp. 185-189, 2000.

[20] J. Schmitt, "OCT elastography: imaging microscopic deformation andstrain of tissue," *Opt. Express*, vol. 3, pp. 199-211, 1998.

[21] S. Gijs van, M. Frits, J. Nico de, and F. W. v. d. S. Anton, "Robust intravascular optical coherence elastography by line correlations," *Phys. Med. Biol.*, vol. 52, p. 2445, 2007.

[22] A. Khalil, R. Chan, A. Chau, B. Bouma, and M. K. Mofrad, "Tissue elasticity estimation with optical coherence elastography: toward mechanical characterization of *in vivo* soft tissue," *Ann. Biomed. Eng.*, vol. 33, pp. 1631-1639, 2005.

[23] J. Rogowska, N. A. Patel, J. G. Fujimoto, and M. E. Brezinski, "Optical coherence tomographic elastography technique for measuring deformation and strain of atherosclerotic tissues," *Heart*, vol. 90, pp. 556-562, 2004.

[24] H. J. Ko, W. Tan, R. Stack, and S. A. Boppart, "Optical coherence elastography of engineered and developing tissue," *Tissue Eng.*, vol. 12, pp. 63-73, 2006.

[25] R. K. Wang, S. Kirkpatrick, and M. Hinds, "Phase-sensitive optical coherence elastography for mapping tissue microstrains in real time," *Appl. Phys. Lett.*, vol. 90, pp. 164105-3, 2007.

[26] S. J. Kirkpatrick, R. K. Wang, and D. D. Duncan, "OCT-based elastography for large and small deformations," *Opt. Express*, vol. 14, pp. 11585-11597, 2006.

[27] B. F. Kennedy, M. Wojtkowski, M. Szkulmowski, K. M. Kennedy, K. Karnowski, and D. D. Sampson, "Improved measurement of vibration amplitude in dynamic optical coherence elastography," *Biomed. Opt. Express*, vol. 3, pp. 3138-3152, 2012.

[28] X. Liang and S. A. Boppart, "Biomechanical properties of *in vivo* human skin from dynamic optical coherence elastography," *IEEE Trans. Biomed. Eng.*, vol. 57, pp. 953-959, 2010.

[29] X. Liang, V. Crecea, and S. A. Boppart, "Dynamic optical coherence elastography: a review," *J. Innov. Opt. Health. Sci.*, vol. 3, pp. 221-233, 2010.

[30] A. L. Oldenburg, V. Crecea, S. A. Rinne, and S. A. Boppart, "Phase-resolved magnetomotive OCT for imaging nanomolar concentrations of magnetic nanoparticles in tissues," *Opt. Express*, vol. 16, pp. 11525-11539, 2008.

[31] A. L. Oldenburg and S. A. Boppart, "Resonant acoustic spectroscopy of soft tissues using embedded magnetomotive nanotransducers and optical coherence tomography," *Phys. Med. Biol.*, vol. 55, pp. 1189-1201, 2010.

[32] A. L. Oldenburg, W. Gongting, D. Spivak, F. Tsui, A. S. Wolberg, and T. H. Fischer, "Imaging and elastometry of blood clots using magnetomotive optical coherence tomography and labeled platelets," *IEEE J. Sel. Top. Quant*, vol. 18, pp. 1100-1109, 2012.

[33] R. K. Wang, Z. Ma, and S. J. Kirkpatrick, "Tissue Doppler optical coherence elastography for real time strain rate and strain mapping of soft tissue," *Appl. Phys. Lett.*, vol. 89, pp. 144103-3, 2006.

[34] R. C. Chan, A. H. Chau, W. C. Karl, S. Nadkarni, A. S. Khalil, N. Iftimia, M. Shishkov, G. J. Tearney, M. R. Kaazempur-Mofrad, and B. E. Bouma, "OCT-based arterial elastography: robust estimation exploiting tissue biomechanics," *Opt. Express*, vol. 12, pp. 4558-4572, 2004.

[35] S. J. Kirkpatrick, R. K. Wang, D. D. Duncan, M. Kulesz-Martin, and K. Lee, "Imaging the mechanical stiffness of skin lesions by *in vivo* acousto-optical elastography," *Opt. Express*, vol. 14, pp. 9770-9, Oct 16 2006.

[36] X. Liang, B. W. Graf, and S. A. Boppart, "Imaging engineered tissues using structural and functional optical coherence tomography," *J. Biophotonics*, vol. 2, pp. 643-55, 2009.

[37] R. K. Manapuram, S. R. Aglyamov, F. M. Monediado, M. Mashiatulla, J. Li, S. Y. Emelianov, and K. V. Larin, "*In vivo* estimation of elastic wave parameters using phase-stabilized swept source optical coherence elastography," *J. Biomed. Opt.*, vol. 17, p. 100501, 2012.

[38] M. R. Ford, W. J. Dupps, Jr., A. M. Rollins, A. S. Roy, and Z. Hu, "Method for optical coherence elastography of the cornea," *J. Biomed. Opt.*, vol. 16, p. 016005, 2011.

[39] S. G. Adie, X. Liang, B. F. Kennedy, R. John, D. D. Sampson, and S. A. Boppart, "Spectroscopic optical coherence elastography," *Opt. Express*, vol. 18, pp. 25519-25534, 2010.

[40] X. Liang, S. G. Adie, R. John, and S. A. Boppart, "Dynamic spectral-domain optical coherence elastography for tissue characterization," *Opt. Express*, vol. 18, pp. 14183-14190, 2010.

[41] B. F. Kennedy, T. R. Hillman, R. A. McLaughlin, B. C. Quirk, and D. D. Sampson, "*In vivo* dynamic optical coherence elastography using a ring actuator," *Opt. Express*, vol. 17, pp. 21762-21772, 2009.

[42] W. Qi, R. Chen, L. Chou, G. Liu, J. Zhang, Q. Zhou, and Z. Chen, "Phase-resolved acoustic radiation force optical coherence elastography," *J. Biomed. Opt.*, vol. 17, p. 110505, 2012.

[43] M. Razani, A. Mariampillai, C. Sun, T. W. H. Luk, V. X. D. Yang, and M. C. Kolios, "Feasibility of optical coherence elastography measurements of shear wave propagation in homogeneous tissue equivalent phantoms," *Biomed. Opt. Express*, vol. 3, pp. 972-980, 2012.

[44] D. D. Duncan and S. J. Kirkpatrick, "Processing algorithms for tracking speckle shifts in optical elastography of biological tissues," *J. Biomed. Opt.*, vol. 6, pp. 418-426, 2001.

[45] K. D. Mohan and A. L. Oldenburg, "Elastography of soft materials and tissues by holographic imaging of surface acoustic waves," *Opt. Express,* vol. 20, pp. 18887-18897, 2012.

[46] D. Huang, E. Swanson, C. Lin, J. Schuman, W. Stinson, W. Chang, M. Hee, T. Flotte, K. Gregory, C. Puliafito, and J. Fujimoto, "Optical coherence tomography," *Science*, vol. 254, pp. 1178-1181, 1991.

[47] A. L. Oldenburg, J. R. Gunther, and S. A. Boppart, "Imaging magnetically labeled cells with magnetomotive optical coherence tomography," *Opt. Lett.*, vol. 30, pp. 747-749, 2005.

[48] O. Junghwan, D. F. Marc, K. Jeehyun, C. Chris, E. Stanislav, and E. M. Thomas, "Detection of magnetic nanoparticles in tissue using magneto-motive ultrasound," *Nanotechnology*, vol. 17, p. 4183, 2006.

[49] A. L. Oldenburg, F. J.-J. Toublan, K. S. Suslick, A. Wei, and S. A. Boppart, "Magnetomotive contrast for *in vivo* optical coherence tomography," *Opt. Express*, vol. 13, pp. 6597-6614, 2005.

[50] R. Kopelman, Y.-E. Lee Koo, M. Philbert, B. A. Moffat, G. Ramachandra Reddy, P. McConville, D. E. Hall, T. L. Chenevert, M. S. Bhojani, S. M. Buck, A. Rehemtulla, and B. D. Ross, "Multifunctional nanoparticle platforms for *in vivo* MRI enhancement and photodynamic therapy of a rat brain cancer," *J. Magn. Magn. Mater.*, vol. 293, pp. 404-410, 2005.

[51] R. John, R. Rezaeipoor, S. G. Adie, E. J. Chaney, A. L. Oldenburg, M. Marjanovic, J. P. Haldar, B. P. Sutton, and S. A. Boppart, "*In vivo* magnetomotive optical molecular imaging using targeted magnetic nanoprobes," *Proc. Natl. Acad. Sci.*, pp. 8085-8090, 2010.

[52] V. Crecea, A. L. Oldenburg, X. Liang, T. S. Ralston, and S. A. Boppart, "Magnetomotive nanoparticle transducers for optical rheology of viscoelastic materials," *Opt. Express*, vol. 17, pp. 23114-23122, 2009.

[53] M. A. Choma, A. K. Ellerbee, C. Yang, T. L. Creazzo, and J. A. Izatt, "Spectral-domain phase microscopy," *Opt. Lett.*, vol. 30, pp. 1162-1164, 2005.

[54] M. A. Choma, A. K. Ellerbee, S. Yazdanfar, and J. A. Izatt, "Doppler flow imaging of cytoplasmic streaming using spectral domain phase microscopy," *J. Biomed. Opt.*, vol. 11, p. 024014, 2006.

[55] C. Joo, T. Akkin, B. Cense, B. H. Park, and J. F. de Boer, "Spectral-domain optical coherence phase microscopy for quantitative phase-contrast imaging," *Opt. Lett.*, vol. 30, pp. 2131-2133, 2005.

[56] M. Sticker, M. Pircher, E. Götzinger, H. Sattmann, A. F. Fercher, and C. K. Hitzenberger, "*En face* imaging of single cell layers by differential phase-contrast optical coherence microscopy," *Opt. Lett.*, vol. 27, pp. 1126-1128, 2002.

[57] M. V. Sarunic, S. Weinberg, and J. A. Izatt, "Full-field swept-source phase microscopy," *Opt. Lett.*, vol. 31, pp. 1462-1464, 2006.

[58] M. H. De la Torre-Ibarra, P. D. Ruiz, and J. M. Huntley, "Double-shot depth-resolved displacement field measurement using phase-contrast spectral optical coherence tomography," *Opt. Express*, vol. 14, pp. 9643-9656, 2006.

[59] B. J. Vakoc, S. H. Yun, J. F. de Boer, G. J. Tearney, and B. E. Bouma, "Phase-resolved optical frequency domain imaging," *Opt. Express*, vol. 13, pp. 5483-5493, 2005.

[60] C. J. Pedersen, S. Yazdanfar, V. Westphal, and A. M. Rollins, "Phase-referenced Doppler optical coherence tomography in scattering media," *Opt. Lett.*, vol. 30, pp. 2125-2127, 2005.

[61] H. Ren, K. M. Brecke, Z. Ding, Y. Zhao, J. S. Nelson, and Z. Chen, "Imaging and quantifying transverse flow velocity with the Doppler bandwidth in a phase-resolved functional optical coherence tomography," *Opt. Lett.*, vol. 27, pp. 409-411, 2002.

[62] Y. Zhao, Z. Chen, C. Saxer, Q. Shen, S. Xiang, J. F. de Boer, and J. S. Nelson, "Doppler standard deviation imaging for clinical monitoring of *in vivo* human skin blood flow," *Opt. Lett.*, vol. 25, pp. 1358-1360, 2000.

[63] H. Ren, Z. Ding, Y. Zhao, J. Miao, J. S. Nelson, and Z. Chen, "Phase-resolved functional optical coherence tomography: simultaneous imaging of *in situ* tissue structure, blood flow velocity, standard deviation, birefringence, and Stokes vectors in human skin," *Opt. Lett.*, vol. 27, pp. 1702-1704, 2002.

[64] B. White, M. Pierce, N. Nassif, B. Cense, B. Park, G. Tearney, B. Bouma, T. Chen, and J. de Boer, "*In vivo* dynamic human retinal blood flow imaging using ultra-high-speed spectral domain optical coherence tomography," *Opt. Express*, vol. 11, pp. 3490-3497, 2003.

[65] H. Ren, T. Sun, D. J. MacDonald, M. J. Cobb, and X. Li, "Real-time *in vivo* blood-flow imaging by moving-scatterer-sensitive spectral-domain optical Doppler tomography," *Opt. Lett.*, vol. 31, pp. 927-929, 2006.
[66] Z. Ding, Y. Zhao, H. Ren, J. Nelson, and Z. Chen, "Real-time phase-resolved optical coherence tomography and optical Doppler tomography," *Opt. Express*, vol. 10, pp. 236-245, 2002.
[67] C. Fang-Yen, M. Chu, H. S. Seung, R. R. Dasari, and M. Feld, "Noncontact measurement of nerve displacement during action potential with adual-beam low-coherence interferometer," *Opt. Lett.*, vol. 29, pp. 2028-2030, 2004.
[68] M. Choma, M. Sarunic, C. Yang, and J. Izatt, "Sensitivity advantage of swept source and Fourier domain optical coherence tomography," *Opt. Express*, vol. 11, pp. 2183-2189, 2003.
[69] R. Leitgeb, C. K. Hitzenberger, and A. F. Fercher, "Performance of Fourier domain vs. time domain optical coherence tomography," *Opt. Express*, vol. 11, pp. 889-894, 2003.
[70] R. A. Leitgeb, W. Drexler, A. Unterhuber, B. Hermann, T. Bajraszewski, T. Le, A. Stingl, and A. F. Fercher, "Ultrahigh resolution Fourier domain optical coherence tomography," *Opt. Express*, vol. 12, pp. 2156-2165, 2004.
[71] J. F. de Boer, B. Cense, B. H. Park, M. C. Pierce, G. J. Tearney, and B. E. Bouma, "Improved signal-to-noise ratio in spectral-domain compared with time-domain optical coherence tomography," *Opt. Lett.*, vol. 28, pp. 2067-2069, 2003.
[72] E. P. Furlani, "Magnetophoretic separation of blood cells at the microscale," *J. Phys. D: Appl. Phys.*, vol. 40, p. 1313, 2007.
[73] V. Crecea, A. L. Oldenburg, T. S. Ralston, and S. A. Boppart, "Phase-resolved spectral-domain magnetomotive optical coherence tomography," in *SPIE (The International Society for Optical Engineering) Photonics West: Biomedical Optics*, San Jose, CA, 2007, pp. 64291X-10.
[74] D. Ouis, "Characterization of polymers by means of a standard viscoelastic model and fractional derivate calculus," *Int. J. Polymer. Mater. Po.*, vol. 53, pp. 633-644, 2004.
[75] D. C. Adler, R. Huber, and J. G. Fujimoto, "Phase-sensitive optical coherence tomography at up to 370,000 lines per second using buffered Fourier domain mode-locked lasers," *Opt. Lett.*, vol. 32, pp. 626-628, 2007.
[76] D. Valtorta and E. Mazza, "Dynamic measurement of soft tissue viscoelastic properties with a torsional resonator device," *Med. Image Anal.*, vol. 9, pp. 481-490, 2005.
[77] X. Liang, A. L. Oldenburg, V. Crecea, E. J. Chaney, and S. A. Boppart, "Optical micro-scale mapping of dynamic biomechanical tissue properties," *Opt. Express*, vol. 16, pp. 11052-11065, 2008.
[78] S. Abbas, B. Jonathan, L. Chris, and B. P. Donald, "Measuring the elastic modulus of *ex vivo* small tissue samples," *Phys. Med. Biol.*, vol. 48, p. 2183, 2003.
[79] P. Agache and P. Humbert, *Measuring the skin*: Springer-Verlag, 2004.
[80] R. John, E. J. Chaney, and S. A. Boppart, "Dynamics of magnetic nanoparticle-based contrast agents in tissues tracked using magnetomotive optical coherence tomography," *IEEE J. Sel. Top. Quant*, vol. 16, pp. 691-697, 2010.
[81] X. Trepat, G. Lenormand, and J. J. Fredberg, "Universality in cell mechanics," *Soft Matter*, vol. 4, pp. 1750-1759, 2008.
[82] B. R. Daniels, B. C. Masi, and D. Wirtz, "Probing single-cell micromechanics *in vivo*: the microrheology of C. elegans developing embryos," *Biophys. J.*, vol. 90, pp. 4712-4719, 2006.
[83] X. Tang, T. B. Kuhlenschmidt, M. S. Kuhlenschmidt, and T. A. Saif, "Mechanical force affects expression of an *in vitro* metastasis-like phenotype in HCT-8 cells," *Biophys. J.*, vol. 99, pp. 2460-2469, 2010.
[84] N. T.-H. Robert D, Gallet F, Wilhelm C, "*In vivo* determination of fluctuating forces during endosome trafficking using a combination of active and passive microrheology," *PLoS ONE*, vol. 5, p. 10046, 2010.
[85] I. De Vlaminck and C. Dekker, "Recent advances in magnetic tweezers," *Annu. Rev. Biophys.*, vol. 41, pp. 453-72, 2012.
[86] E. J. McDowell, A. K. Ellerbee, M. A. Choma, B. E. Applegate, and J. A. Izatt, "Spectral domain phase microscopy for local measurements of cytoskeletal rheology in single cells," *J. Biomed. Opt.*, vol. 12, pp. 044008-11, 2007.
[87] N. Wang, J. P. Butler, and D. E. Ingber, "Mechanotransduction across the cell surface and through the cytoskeleton " *Science*, vol. 260, pp. 1124-1127, 1993.

[88] A. R. Bausch, W. Möller, and E. Sackmann, "Measurement of local viscoelasticity and forces in living cells by magnetic tweezers," *Biophys. J.*, vol. 76, pp. 573-579, 1999.
[89] B. W. Graf, S. G. Adie, and S. A. Boppart, "Correction of coherence gate curvature in high numerical aperture optical coherence imaging," *Opt. Lett.*, vol. 35, pp. 3120-3122, 2010.
[90] B. W. Graf and S. A. Boppart, "Multimodal *in vivo* skin imaging with integrated optical coherence and multiphoton microscopy," *IEEE J. Sel. Top. Quantum Electron.*, vol. 18, pp. 1280-1286, 2012.
[91] B. W. Graf, Z. Jiang, H. Tu, and S. A. Boppart, "Dual-spectrum laser source based on fiber continuum generation for integrated optical coherence and multiphoton microscopy," *J. Biomed. Opt.*, vol. 14, p. 034019, 2009.
[92] R. John, F. T. Nguyen, K. J. Kolbeck, E. J. Chaney, M. Marjanovic, K. S. Suslick, and S. A. Boppart, "Targeted multifunctional multimodal protein-shell microspheres as cancer imaging contrast agents," *Mol. Imaging. Biol.*, vol. 14, pp. 17-24, 2011.
[93] C. Vinegoni, T. S. Ralston, W. Tan, W. Luo, D. L. Marks, and S. A. Boppart, "Integrated structural and functional optical imaging combining spectral-domain optical coherence and multiphoton microscopy," *Appl. Phys. Lett.*, vol. 88, pp. 053901-3, 2006.
[94] G. Popescu, T. Ikeda, R. R. Dasari, and M. S. Feld, "Diffraction phase microscopy for quantifying cell structure and dynamics," *Opt. Lett.*, vol. 31, pp. 775-777, 2006.
[95] H. Ding and G. Popescu, "Instantaneous spatial light interference microscopy," *Opt. Express*, vol. 18, pp. 1569-1575, 2010.
[96] Y. Liu, Z. Chen, and J. Wang, "Systematic evaluation of biocompatibility of magnetic Fe_3O_4 nanoparticles with six different mammalian cell lines," *J. Nanopart. Res.*, vol. 13, pp. 199-212, 2011.
[97] Y. Zhang, N. Kohler, and M. Zhang, "Surface modification of superparamagnetic magnetite nanoparticles and their intracellular uptake," *Biomaterials*, vol. 23, pp. 1553-1561, 2002.
[98] K. M. Kamruzzaman Selim, Y.-S. Ha, S.-J. Kim, Y. Chang, T.-J. Kim, G. Ho Lee, and I.-K. Kang, "Surface modification of magnetite nanoparticles using lactobionic acid and their interaction with hepatocytes," *Biomaterials*, vol. 28, pp. 710-716, 2007.
[99] J. Lim, C. Lanni, E. R. Evarts, F. Lanni, R. D. Tilton, and S. A. Majetich, "Magnetophoresis of Nanoparticles," *ACS Nano*, vol. 5, pp. 217-226, 2010.
[100] J. Gao, W. Zhang, P. Huang, B. Zhang, X. Zhang, and B. Xu, "Intracellular Spatial Control of Fluorescent Magnetic Nanoparticles," *J. Am. Chem. Soc.*, vol. 130, pp. 3710-3711, 2008.
[101] J. Kanger, V. Subramaniam, and R. van Driel, "Intracellular manipulation of chromatin using magnetic nanoparticles," *Chromosome Res*, vol. 16, pp. 511-522, 2008.
[102] A. H. B. de Vries, B. E. Krenn, R. van Driel, and J. S. Kanger, "Micro Magnetic Tweezers for Nanomanipulation Inside Live Cells," *Biophys. J.*, vol. 88, pp. 2137-2144, 2005.
[103] B. D. Matthews, D. R. Overby, F. J. Alenghat, J. Karavitis, Y. Numaguchi, P. G. Allen, and D. E. Ingber, "Mechanical properties of individual focal adhesions probed with a magnetic microneedle," *Biochem. Biophys. Res. Commun.*, vol. 313, pp. 758-764, 2004.
[104] B. Fabry, G. N. Maksym, J. P. Butler, M. Glogauer, D. Navajas, N. A. Taback, E. J. Millet, and J. J. Fredberg, "Time scale and other invariants of integrative mechanical behavior in living cells," *Phys Rev E*, vol. 68, p. 041914, 2003.
[105] B. Fabry, G. N. Maksym, J. P. Butler, M. Glogauer, D. Navajas, and J. J. Fredberg, "Scaling the Microrheology of Living Cells," *Phys. Rev. Lett.*, vol. 87, p. 148102, 2001.
[106] E. J. McDowell, A. K. Ellerbee, M. A. Choma, B. E. Applegate, and J. A. Izatt, "Spectral domain phase microscopy for local measurements of cytoskeletal rheology in single cells," *J. Biomed. Opt.*, vol. 12, pp. 044008-11, 2007.